Androgen receptor imprints satellite cells stemness and preserves their reservoir for lifelong regeneration and optimal repair

Joe G. Rizk[1*], Kamar C. Ghaibour[1*], Sirine Souali-Crespo[1], Emilia Calvano[1], Aurore Bilger[1], Hugues Jacobs[1], Nadia Messaddeq[1], Qingshuang Cai[1], Erwan Grangirard[1], Rajesh Sahu[1], Arnaud Ferry[2], Valentin Fourcade[3], Joffrey Zoll[3], Gianni Zanardelli[1], Nacho Molina[1], Coralie Fontaine[4], Jean-François Arnal[4], Daniel Metzger[1], Delphine Duteil[1#]

[1] Université de Strasbourg, CNRS, Inserm, IGBMC UMR 7104- UMR-S 1258, F-67400 Illkirch, France

[2] Centre de Recherche en Myologie, UMRS974-Sorbonne Université-INSERM U974-Association Institut de Myologie, France.

[3] Université de Strasbourg, Centre de recherche en biomédecine de Strasbourg, UMR 3072, Strasbourg, France

[4] Institut National de la Santé et de la Recherche Médicale (INSERM), U1297, Institut des Maladies Métaboliques et Cardiovasculaires (I2MC), Université Toulouse III Paul Sabatier, CHU Rangueil (University Hospital) de Toulouse, F-31432 Toulouse, France

[#] Author to whom correspondence should be addressed at duteild@igbmc.fr.

[*] These authors equally contributed to this work.

SUMMARY

Skeletal muscle stem cells (MuSC) are the guardians of muscle regeneration, sustaining tissue integrity through a delicate balance of quiescence, activation, and lineage commitment. While numerous molecular cues have been implicated in regulating these processes, the influence of androgen receptor (AR) signaling, an essential hormonal pathway for male muscle physiology, has remained largely unexplored. Here, we show that AR expression defines quiescent MuSC and acts as a safeguard of their dormancy. Integrated multi-omic analyses reveal a redistribution of AR binding from quiescence-maintenance loci to regulatory elements driving activation and metabolic reprogramming during repair. Loss of AR in young adult mice disrupts this balance, precipitating premature cell-cycle entry, skewed division modalities, depletion of the stem cell reservoir, and destabilization of the niche. These defects converge with hallmarks of aging-associated androgen decline, while androgen supplementation restores regenerative competence. Together, our findings establish AR signaling as a pivotal determinant of MuSC fate and a cornerstone of skeletal muscle homeostasis.

KEY WORDS

Satellite Cells, Androgen Receptor, Androgens, Skeletal Muscle, Regeneration, Ageing, Symmetric differentiation

38 **INTRODUCTION**

39 Skeletal muscles exhibit a remarkable regeneration capacity upon injury, resulting from the fusion of
40 newly formed myocytes to generate myofibers that replace the damaged ones. This process is initiated
41 by myofiber degeneration, causing inflammatory cell infiltration followed by the activation of satellite
42 cells, which are the muscle stem cells (MuSC) [1]. In the intact muscle, MuSC reside in a quiescent state
43 within a specialized niche between the myofiber sarcolemma and the basal lamina [2, 3]. They are
44 defined by the expression of the myogenic transcription factor paired box 7 (*Pax7*), a key marker of
45 their identity and function [4].

46 Upon muscle injury, MuSC exhibit a dual capacity. They can either self-renew to replenish the stem
47 cell pool and preserve long-term regenerative competence, or enter a proliferative phase followed by
48 activation of the myogenic differentiation program, culminating in fusion and formation of new
49 myofibers [5, 6]. These key myogenic features, are intrinsically dependent on MuSC microenvironment,
50 comprising immune and stromal cells. This microenvironment is tightly regulated by interactions with
51 extracellular matrix components, inter-cell signaling and paracrine or endocrine stimuli [7-9]. With age,
52 skeletal muscle regenerative capacities progressively decline, which has been recently attributed to a
53 reduction in MuSC number and function [10-12]. These processes are thought to be exacerbated by
54 hormonal changes, including decrease in circulating androgens [13-15].

55 Androgens are steroid hormones mainly produced by male gonads. They play a crucial role in
56 modulating muscle homeostasis and MuSC fate, both during postnatal development and at adult
57 stages [16, 17]. In young adult mice, androgens promote MuSC quiescence through a Notch-dependent
58 pathway [18], and influence their activation, proliferation, and differentiation [18-20]. In addition, androgen
59 supplementation increases MuSC numbers in both animal models and humans [21]. Oppositely,
60 castration-induced androgen deprivation in rodents leads to perturbed MuSC homeostasis [22].
61 Androgens exert their effects through the androgen receptor (AR), a ligand-activated transcription
62 factor and member of the nuclear receptor superfamily, which upon ligand binding translocates to the
63 nucleus and binds specific DNA sequences known as androgen response elements (AREs), to regulate
64 target genes expression [23-25]. We previously showed that AR in myofibers is instrumental for the
65 musculoskeletal system by controlling gene networks required for structural and metabolic demands
66 [25, 26]. Nevertheless, the role of androgens *via* AR in MuSC during muscle regeneration, the broader
67 consequences of androgen-dependent decline on the regenerative machinery, the underlying
68 molecular mechanisms, and its potential causal link to age-associated muscle degeneration remain to
69 be fully elucidated.

70 By integrating genome-wide profiling and histological analysis, with the study of an inducible MuSC-
71 specific AR knockout mouse model and stem-like myogenic cell lines, we delineate the molecular

72 mechanisms through which androgens *via* their receptor regulate MuSC regenerative functions. Our
73 findings highlight the pivotal role of MuSC-AR in muscle repair, identifying AR-dependent stem cell
74 profiles and supportive MuSC subtypes involved in postnatal myogenesis. We further reveal that AR
75 orchestrates stemness transitions by sequential chromatin repositioning following injury, thereby
76 controlling gene networks governing MuSC self-renewal, proliferation, and differentiation.
77 Additionally, we demonstrate that androgen signaling contributes to the age-related decline in muscle
78 healing capacities, and validate the translational relevance of murine findings in human myoblasts.

79 **RESULTS**

80 **AR deficiency in MuSC in young individuals compromises regenerative capacity and alters metabolic**
81 **and structural transcriptional programs in skeletal muscle**

82 To dissect the age-dependent role of AR signaling within MuSC, we generated mice with a conditional
83 AR deletion in this cell lineage (hereafter $AR^{(i)sat-/Y}$ mice). Nine-week-old mice harboring floxed *Ar*
84 alleles and expressing the *Pax7*-$CreER^{T2}$ transgene were treated with tamoxifen (TAM) for 5 days,
85 enabling selective deletion of *Ar* in MuSC (Figures S1A-S1D). TAM-treated littermates lacking the *Pax7*-
86 $CreER^{T2}$ transgene served as controls. To evaluate the functional consequences of AR ablation on
87 skeletal muscle regenerative capacities, we subjected young (3-month-old) control and $AR^{(i)sat-/Y}$ mice
88 to acute Tibialis Anterior (TA) muscle injury *via* cardiotoxin (CTX) injection one month after gene
89 ablation, and assessed histological features of repair at 5-, 7-, 14-, 28- and 42-days post-injury (dpi).
90 While no gross phenotypical abnormalities were noticed in the absence of injury (Figures S1E-S1G), At
91 5 dpi, a timepoint at which MuSC activation and early differentiation culminate [27], both genotypes
92 showed similar hallmarks of effective regeneration, including centronucleated fibers, necrosis, and
93 immune cell infiltration (Figure S1H). However, at 7 dpi, $AR^{(i)sat-/Y}$ mice exhibited regenerative defects,
94 including persistent inflammation, and aberrant fiber morphology that persisted until 42 dpi, that
95 were not due to the $CreER^{T2}$ knock-in (Figures 1A and S1H). Ultrastructural analyses performed at 7
96 dpi, a timepoint at which mononuclear cells fuse in order to form myosyncytia and primary
97 regenerative outcomes are captured [28], revealed that $AR^{(i)sat-/Y}$ muscles displayed disorganized
98 sarcomeres, with misaligned triads characterized by dilated T-tubules, disrupted Z-lines, and poorly
99 defined or absent M-lines (Figure 1B). These structural muscle defects correlated with a significant
100 reduction in myofiber cross-sectional area (Figure 1C), which translated into a significant reduction in
101 contractile force at 28 dpi (Figure 1D). Muscle dysfunction was accompanied by a marked reduction
102 in the MuSC pool at 7 dpi (Figures 1E and 1F), which persisted at 28 dpi (Figures S1I and S1J), showing
103 that loss of AR in MuSC severely impairs regenerative capacity in young male mice.

104 To elucidate AR transcriptional landscape, we conducted bulk RNA sequencing (RNA-seq) on TA
105 muscles harvested at 7 dpi from young $AR^{(i)sat-/Y}$ and control mice. Our analysis revealed a differential
106 expression of 3,586 genes, comprising 2,045 downregulated and 1,541 upregulated genes in AR-
107 deficient mice (Figures 1G and S1K). Pathway analyses of the downregulated genes highlighted a
108 strong association with biological processes involved in actin cytoskeleton organization, focal
109 adhesion, and developmental signaling cascades such as the PI3K-Akt pathway (Figure 1H). Strikingly,
110 the expression of key myogenic regulators, including *Pax7*, *Myf5*, *Myod1*, *Myog*, fusion-mediating
111 factors such as *Myomixer* (*Mymx*) and *Myomaker* (*Mymk*) was markedly reduced in $AR^{(i)sat-/Y}$ muscles
112 (Figure 1I), in agreement with the decreased MuSC number. Similarly, transcripts encoding contractile

113 cytoskeletal components such as actin, actinin, troponin and tropomyosin isoforms (e.g. *Actb*, *Actn1*,
114 *Actn4*, *Tnnc1*, *Tnnt2*, *Tpm3*), and embryonic myosin heavy chains isoforms (*Myh3*, embryonic and
115 *Myh8*, perinatal), as well as non-contractile components, including laminins (*Lmna*), *Myomesin 3*
116 (*Myom3*), and *Dystrophin* (*Dmd*), were significantly diminished (Figures 1G and 1I), providing a
117 molecular rationale for the morphological abnormalities observed at this timepoint. In agreement,
118 immunofluorescence analysis of DMD at 7 dpi revealed profound structural abnormalities in $AR^{(i)sat-/Y}$
119 mice compared to control littermates (Figure 1J). Moreover, co-staining for sarcomeric alpha actinin
120 (ACTN1) and DMD on transverse sections showed disrupted sarcomere alignment and uneven ACTN1
121 distribution in mutant fibers, while longitudinal sections confirmed major striation defaults (Figure 1K,
122 pink arrows). Notably, whereas healing control fibers had centrally positioned nuclei, $AR^{(i)sat-/Y}$ fibers
123 showed disorganized central nuclear localization (Figure 1K, white arrows), reflecting a disrupted
124 cytoskeletal organization. Consistent with our transcriptomic data, immunostaining for embryonic
125 myosin heavy chain (MYH3) at 5 and 7 dpi showed a ~50% reduction in the number of MYH3-positive
126 fibers in $AR^{(i)sat-/Y}$ mice compared to controls (Figures 1L and 1M), signifying delayed or incomplete
127 myogenic progression. To further investigate this impairment, we examined the expression profile of
128 myosin heavy chain isoforms (Figure 1N). In contrast to the downregulation of *Myh3* and *Myh8*,
129 transcripts of *Myh2*, *Myh4*, and *Myh7* (encoding MyHC IIa, IIb, and I, respectively) were upregulated
130 (Figure 1N), reflecting a shift toward increased expression of adult myosin heavy chain isoforms at the
131 expense of fetal ones, although *Myh1* (MyHC IIx) did not reach statistical significance (Figure 1N).
132 Interestingly, transcriptomic analysis of the 1,541 genes upregulated in 7 dpi-injured $AR^{(i)sat-/Y}$ TA
133 muscles revealed a predominant enrichment in metabolic pathways, particularly those governing
134 glycolysis, oxidative phosphorylation, mitochondrial function, and the metabolism of glycogen, fatty
135 acids, and amino acids (Figure 1H). Notably, expression of several key regulators of cellular
136 metabolism, including aconitase 2 (*Aco2*), citrate synthase (*Cs*), and multiple isoforms of isocitrate
137 dehydrogenase (e.g. *Idh2* and *Idh3a*), was markedly elevated in $AR^{(i)sat-/Y}$ muscles. This was paralleled
138 by increased expression of genes and components of the oxidative phosphorylation machinery,
139 including most of the members of mitochondrial complex I (e.g., *Ndufa1-13*), II (e.g., *Sdha-d*), III (e.g.,
140 *Uqcrc1-2*), IV (e.g., *Cox5a*, and *Cox10a*), and V (e.g., *Atp5a1* and *Atp5b*) (Figure 1O). Of note, the
141 expression of these genes was not affected in the absence of injury (Figures S1L and S1M).
142 To investigate whether the absence of MuSC-AR during regeneration promotes a metabolic shift
143 toward a more oxidative muscle fiber phenotype, we stained NADH dehydrogenase activity (NADH-
144 DH) 7 dpi. In regenerating TA muscles from control mice, we observed lightly stained fibers, indicative
145 of glycolytic metabolism. In contrast, $AR^{(i)sat-/Y}$ muscles displayed a higher presence of darkly stained
146 fibers (Figure 1P), reflecting increased NADH-DH activity. These findings were corroborated by

147 cytochrome c oxidase (COX) activity staining, indicative of a glycolytic-to-oxidative shift in fiber type
148 composition (Figure 1P). These findings prompted us to investigate whether such metabolic
149 alterations are intrinsically rooted in MuSC. Seahorse analysis performed on LHCN-M2 human
150 myoblasts, treated with 100 nM of the AR antagonist flutamide, unveiled an increased oxidative
151 phosphorylation activity when compared to vehicle-treated cells (Figures 1Q and S1N) indicating that
152 the metabolic abnormalities observed in regenerating myofibers may originate from intrinsic defects
153 in MuSC. In parallel, basal ECAR was measured for glycolysis analyses (Figures S1O and S1P).
154 Altogether, our data show that AR loss in young individuals leads to MuSC depletion and important
155 structural defects, associated with a fiber-type switch towards oxidative metabolism.
156
157 **Androgen signaling in MuSC coordinates gene programs essential for homeostasis and regeneration**
158 To elucidate the cell-specific AR-dependent molecular mechanisms governing MuSC homeostasis
159 during skeletal muscle regeneration, we performed a SMART-seq on FACS-isolated MuSC from 7 dpi-
160 injured TA of young (15-week-old) control and $AR^{(i)sat-/Y}$ male mice. Transcriptomic analysis revealed
161 differential expression of 821 genes in AR-deficient MuSC, including 327 down- and 494 upregulated
162 genes (Figures 2A and S2A). Consistent with the Seahorse assay findings and the histological evidence
163 of a metabolic shift toward oxidative metabolism at 7 dpi, analysis of the upregulated genes
164 highlighted a strong enrichment of pathways related to metabolic processes, particularly cellular
165 respiration and oxidative phosphorylation (Figure 2B). In particular, the expression of *Cox5b* and
166 *Cox6b1*, in addition to numerous genes implicated in mitochondrial homeostasis, was significantly
167 elevated in $AR^{(i)sat-/Y}$ MuSC (Figure 2C). Conversely, pathway analysis of the downregulated gene set
168 revealed a significant association with cell cycle regulation (e.g., DNA replication and cell division)
169 (Figures 2B and 2D).
170 To identify the direct transcriptional targets of AR, we isolated MuSC from TA muscles of control mice
171 by FACS at 7 dpi, and performed CUT&RUN assays using AR-specific antibodies, alongside profiling of
172 demethylated histone H3 (H3K4me2), a well-established marker of active promoters and enhancers.
173 Bioinformatic analysis identified 7,346 AR-binding peaks, predominantly located within intronic and
174 intergenic regions encompassing the canonical androgen response elements (AREs) (Figures 2E and
175 S2B), as well as 39,900 peaks associated with the H3K4me2 mark, evenly distributed between
176 promoter, intron and intergenic regions (Figure S2C). Integrative analysis of the two datasets revealed
177 that AR is directly recruited to 3,104 transcribed genes (Figure S2D). Gene ontology and pathway
178 enrichment analyses of AR-bound genes uncovered a strong association with key developmental and
179 regenerative pathways, including the HIPPO (e.g. *Tead1*, *Wwc1*, *Fat4*) and WNT signaling cascades
180 (e.g. *Wnt5a*, *Fzd4*), as well as signaling modules related to tissue remodeling and regeneration, such

181 as cell adhesion, focal adhesion, extracellular matrix (ECM)-receptor interactions, and actin
182 cytoskeleton regulation (Figure 2F). Notably, AR occupancy was also observed at genes essential for
183 stem cell homeostasis (e.g. *Foxo1*, *Bcl2*), muscle repair (e.g. *Mstn*, *Cxcl2*, *Cdh15*), and sarcomere
184 assembly or function (e.g. *Myh1*, *Mylk4*, *Myom2*). A transcription start site (TSS) gene-centric analysis
185 demonstrated that AR binds more than the two-thirds of both down- and upregulated genes in $AR^{(i)sat-}$
186 $^{/Y}$ mice within a 100-kb window (Figure 2G), showing that AR predominantly regulates gene expression
187 through distal elements. Representative AR binding loci within key genes involved in the
188 aforementioned pathways, including *Ar* itself, *Fzd4*, *Kdmc4*, *Myh1, Tead1*, and *Mylk4* are illustrated in
189 Figure 2H. Gene ontology analysis revealed that genes downregulated in association with AR peaks at
190 7 dpi were predominantly involved in cellular structural and organelle-related processes (Figure S2E),
191 whereas upregulated genes were enriched in metabolic pathways (Figure S2F), thereby providing a
192 molecular basis for the impaired phenotype observed at the histological level. Altogether, these
193 findings support a model in which AR orchestrates regenerative transcriptional programs in MuSC via
194 enhancer-driven mechanisms.
195

196 **Single-cell RNA sequencing reveals early molecular and cellular alterations in the AR-deficient MuSC**
197 **microenvironment**

198 To decipher the primary events underlying defective MuSC homeostasis caused by AR loss, and the
199 consequent impact on their microenvironment during impaired regeneration, we performed single-
200 cell RNA sequencing (scRNA-seq) in 5-dpi-injured TA muscles of young (15-week-old) control and
201 $AR^{(i)sat-/Y}$ mice (Figure S3A). Of note, $AR^{(i)sat-/Y}$ mice harbored the YFP transgene selectively in MuSC to
202 efficiently follow those cells. We identified 12 unsupervised clusters, annotated to the literature [29, 30],
203 based on the expression of specific marker genes (Figures 3A, S3A and S3B), with no evidence of cell
204 population loss or emergence in mutants (Figures 3A, 3B and Table S1 and S2). However, we observed
205 a slight reduction in the proportion of fibro-adipogenic progenitors (FAPs) and MuSC, as well as an
206 increase in that of both macrophages in $AR^{(i)sat-/Y}$ mice compared to controls (Figure 3B). Flow
207 cytometry analysis of injured TA muscles at 5 dpi, furtherly confirmed a ~30% increase in macrophages
208 number among $CD45^{+}$ immune cells (Figure 3C), and immunolabeling for F4/80 revealed an upward
209 trend in macrophage abundance (Figure S3C and S3D). In parallel, flow cytometry analysis indicated
210 an ~8% decrease in MuSC, while total immune cells and FAPs were not significantly altered (Figure
211 3D). Notably, *Ar* expression was not ubiquitous across all populations; rather, it was predominantly
212 detected in cell types exhibiting stem-like properties or mesenchymal profiles, including FAPs,
213 fibroblasts, and MuSC (Figure 3E). *Ar* expression was completely abolished in mutant MuSC, and not
214 in other cell types (Figure 3E), while *Yfp* was exclusively expressed in MuSC of $AR^{(i)sat-/Y}$ mice, consistent

215 with the genetic engineering of our model (Figure S3E). Moreover, AR deficiency in MuSC strongly
216 altered the transcriptional profile of their cellular microenvironment (Figure S3F).
217 To assess intercellular communication within injured muscle tissue at 5 dpi, we employed CellChat
218 analysis on scRNA-seq data. In control mice, this analysis revealed a highly interconnected signaling
219 network encompassing all cellular populations, indicative of active and coordinated crosstalk during
220 the regenerative process (Figures S3G and S3H). Interestingly, communication within the MuSC
221 population was diminished in $AR^{(i)sat-/Y}$ mice, as indicated by the decrease of the arrow thickness (Figure
222 3F), pointing to a disruption in intra-population signaling.
223 Given the critical interplay between MuSC, macrophages, and FAPs, we next examined the gene
224 networks affected by MuSC-AR loss within these two cell populations. Functional enrichment analysis
225 of the 1,707 differentially expressed genes upon AR loss in MuSC within macrophages uncovered a
226 transcriptional landscape indicative of macrophages homeostasis (Figure S3I). In particular, transcripts
227 encoding core components of the inflammasome pathway, including caspase 1 (*Casp1*) and its adaptor
228 *Pycard*, were elevated, alongside the chemokines C-C motif chemokine ligand 2 (*Ccl2*) and C-X-C motif
229 chemokine ligand 10 (*Cxcl10*), both of which are known to promote monocyte recruitment.
230 Furthermore, we observed enrichment in metabolic and proteasome pathways intimately linked with
231 immune regulation and tissue remodeling, including oxidative phosphorylation (e.g., *Cox6b1, Cox17*),
232 and ubiquitin-proteasome mediated degradation (e.g., *Uba3*) (Figure S3I). Moreover, macrophage
233 polarization analysis revealed robust expression of canonical pro-inflammatory markers including *Il1b*
234 and *Tnf*, in both control and mutant macrophages at 5 dpi (Figure 3G). In contrast, macrophages from
235 $AR^{(i)sat-/Y}$ mice expressed anti-inflammatory markers such as interleukin-10 (*Il10*) and peroxisome
236 proliferator-activated receptor gamma (*Pparg*) (Figure 3H), suggesting a precocious transition toward
237 an anti-inflammatory phenotype in mutant individuals. Further subclustering of the macrophage
238 population revealed that they did not constitute a homogeneous cluster, but instead, segregate into
239 five transcriptionally distinct subpopulations with specialized functional programs (Figures S3J-S3M).
240 Cluster 0 was characterized by high expression of pro-inflammatory markers such as *Ccr2*, *Il1b*, and
241 *Ccl5*, consistent with recently recruited, monocyte-derived macrophages (Figures S3J-S3L). Cluster 1
242 displayed a strong pro-inflammatory profile, marked by elevated expression of *Tnf*, *Ccl2*, *Ccl7*,
243 *Cxcl1/2/3*, interferon-stimulated genes (*Ifit1/2/3*), indicative of highly activated macrophages involved
244 in leukocyte recruitment and inflammatory amplification (Figures S3J-S3L). Cluster 2 corresponded to
245 phagocytic and lipid-associated macrophages, expressing canonical LAM markers including *Gpnmb*,
246 *Ctsd*, *Spp1*, *Fabp5*, *Lgals3*, and *Cd36*, suggesting a central role in debris clearance and lipid handling
247 during tissue remodeling (Figures S3J-S3L). Cluster 3 was enriched for genes involved in iron
248 metabolism and oxidative stress responses, such as *Slc40a1*, *Hmox1*, *Fth1*, and *Ftl1*, together with

249 *Marco*, *Spic*, and *Arg1*, consistent with specialized macrophages implicated in iron recycling and stress
250 adaptation (Figures S3J-S3L). Finally, Cluster 4 exhibited a tissue-resident, reparative phenotype
251 characterized by *Cd163*, *Lyve1*, *Mrc1*, *Retnla*, and *Folr2* expression, alongside extracellular matrix and
252 remodeling genes including *Col1a1*/2, *Sparc*, and *Gas6*, indicating anti-inflammatory, pro-reparative
253 functions (Figures S3J-S3L). Differential expression analysis across different populations further
254 revealed cluster-specific functional alterations, with altered antigen-presenting capacity, impaired
255 oxidative metabolism, and shifts toward migratory or scavenger states depending on the
256 subpopulation (Figure S3L). scRNA-seq analysis of macrophage populations revealed an increased
257 representation of an anti-inflammatory macrophage subcluster in $AR^{(i)sat-/Y}$ muscles (Figure S3M). To
258 further examine this observation at the injury site, we performed immunofluorescence labeling for
259 CD163, a marker associated with anti-inflammatory, pro-reparative macrophages. Quantification
260 revealed an increase in CD163 mean fluorescence intensity (MFI) in $AR^{(i)sat-/Y}$ TA muscles at 5 dpi
261 compared to controls (Figures S3N and S3O). These observations are consistent with our single-cell
262 RNA sequencing analysis, which identified a macrophage cluster enriched for *Cd163*, *Mrc1*, and *Folr2*
263 expression, indicative of tissue-resident, anti-inflammatory, and remodeling-associated macrophages
264 (Figures S3J and S3K).
265 To determine whether this aberrant immune environment persists over time, we extended our
266 analysis to 7 dpi. Flow cytometry revealed a three-fold increase in immune cells in $AR^{(i)sat-/Y}$ TA relative
267 to controls (Figure 3I), and immunofluorescent labeling of the macrophage-specific marker F4/80
268 exhibited an increasing trend of the signal (Figures 3J, white arrows, and 3K). Remarkably,
269 macrophages were frequently localized inside degenerating muscle fibers of $AR^{(i)sat-/Y}$ mice (Figure 3J,
270 red arrows, and 3K), a phenomenon typically restricted to early regenerative stages, thus indicating
271 delayed resolution of inflammation or prolonged clearance of necrotic tissue. CD163 levels were
272 comparable between $AR^{(i)sat-/Y}$ and control muscles, in contrast to the increased signal observed in
273 mutants at 5 dpi (Figures S3N and S3O). This temporal pattern may suggest that macrophages in $AR^{(i)sat-}$
274 $^{/Y}$ muscles transiently acquire reparative features at earlier stages of regeneration.
275 Together, these findings reveal that AR signaling in MuSC plays a pivotal role in modulating the
276 inflammatory response within the injured muscle by impacting the macrophage transcriptomic
277 repertoire.
278 To unravel the impact of AR loss in MuSC on FAPs transcriptional signature, we performed further
279 functional enrichment analysis of their 976 differentially expressed genes (Figure S3F). Pathway
280 analysis revealed upregulation of fibrosis-related transcripts, including *Tgfb*, alongside extracellular
281 matrix (ECM) remodeling enzymes, such as *Adamts* isoforms, *Mmp19*, *Serpine1*, and *Cthrc1*.
282 Moreover, we observed enhanced expression of key adipogenic regulators (*Zeb1*, *Cebpd*, *Socs1*, and

283 *Socs3*). Functional enrichment also highlighted disruptions in metabolic pathways, notably oxidative
284 phosphorylation (*Cox4i1*, *Cox5a*, *Cox6a1*) and aerobic respiration (*Aco2*, *Hadhb*, *Gls*, *Lipa*) (Figure S3P),
285 pointing toward a shift in FAPs identity, from pro-regenerative to fibrotic and adipogenic.
286 Interestingly, while FAPs numbers were comparable between genotypes at 5 dpi (Figure 3D), a two-
287 fold reduction was observed in $AR^{(i)sat-/Y}$ muscles by 7 dpi (Figure 3I). We therefore postulated that
288 decline might be attributed to differentiation of FAPs towards the fibrogenic or adipogenic lineages.
289 To this aim, we performed Sirius Red staining at 7 dpi on injured TA from control and mutant mice.
290 Mutant muscles displayed a marked increase in collagen deposition, with fibrotic area nearly doubled
291 compared to controls (Figures 3L and 3M, black arrows). These findings were corroborated by
292 Masson's Trichrome staining, which revealed a significant enrichment of collagen within the ECM at 7
293 dpi, with signs of early deposition already evident at 5 dpi in young $AR^{(i)sat-/Y}$ mice (Figure S3Q).
294 Polarized light microscopy revealed that the qualitative composition of the ECM, including collagenous
295 components such as collagens type I (Figures 3L, white arrows and 3N) and III (Figures 3L, cyan blue
296 arrows and 3N), and non-collagenous cones (e.g., fibronectin, laminins, elastin, tenascin-C, and
297 proteoglycans) remained comparable between genotypes, indicating a quantitative rather than
298 compositional remodeling. We further evaluated adipogenic conversion via perilipin-1 (PLIN1)
299 immunostaining. At 5 dpi, $AR^{(i)sat-/Y}$ muscles already showed early signs of adipocyte emergence, which
300 further increased by 7 dpi, whereas control muscles remained largely devoid of PLIN1-positive cells
301 (Figures 3O and 3P). Thus, our data demonstrate that AR loss in MuSC impacts FAPs differentiation
302 capacities promoting fibrosis and adipogenesis.
303 Altogether, these results indicate that AR signaling in MuSC plays a central role in coordinating the
304 regenerative niche by regulating the balance between pro- and anti-inflammatory immune responses
305 and controlling FAP fate (Figure 3Q).
306
307 **AR deficiency in MuSC at young age perturbs their stemness signatures, disrupts their commitment,**
308 **and impairs their differentiation potential**
309 Strikingly, only few genes were differentially expressed in MuSC, suggesting that different cell
310 populations might lay in this cluster (Figure S3F). To further explore the transcriptional changes
311 between control and $AR^{(i)sat-/Y}$ MuSC, we performed subclustering of MuSC following additional
312 stringent quality control, yielding a final dataset of 445 MuSC (Figures S4A and S4B). Unsupervised
313 clustering revealed six distinct MuSC subpopulations (Figure S4B), of which two clusters exhibited an
314 immune signature characterized by the expression of *C1qc*, *Lyz2*, and *Cd68* (Figures S4B and S4C).
315 Given recent findings describing these subsets as immuno-myoblasts in regenerating muscle [29, 31], we
316 hypothesized that these clusters represent MuSC targeted for immune-mediated clearance.

317 Consequently, we excluded these populations from our analysis and re-clustered the remaining four
318 subtypes based on their transcriptional profiles (Figures 4A, S4D, S4E and Table S3).
319 Our analysis delineated two distinct clusters of quiescent MuSC (clusters 0 and 1), both characterized
320 by the expression of *Pax7* and *Myf5*, while lacking *Myod1* and *Myog* expression (Figures 4A, 4B and
321 S4E). Moreover, we identified an activated MuSC subcluster (cluster 2) distinguished by the additional
322 expression of *Myod1* and the proliferation marker *Mki67* (Figures 4A, 4B and S4E). Importantly, a fully
323 committed myogenic cell population (cluster 3), characterized by *Myog* expression as well as that of
324 *Mymk* and *Mymx,* and originally absent in control individuals, emerged in mutant mice (Figures 4A,
325 4B, S4E, and S4F). In line with this observation, we found that *Ar* expression was confined to quiescent
326 clusters 0 and 1 in control mice, whereas ectopic *Myf5* and *Myod1* expression was noted in cluster 1
327 in $AR^{(i)sat-/Y}$ individuals (Figure 4B), indicating that loss of AR in MuSC promotes myogenic commitment.
328 Notably, several genes associated with symmetric division, including *Bmi1*, *Msi2*, and *Zfx*, were
329 upregulated in mutant mice within cluster 3 (Figure S4G), alongside a broader expression of the
330 fusogenic markers *Mymk* and *Mymx* across a larger subset of cells (Figure S4F), indicative of symmetric
331 differentiation.
332 To provide evidence of commitment defaults caused by loss of AR in MuSC, we assessed cell cycle
333 distribution within each cluster (Figures 4C and S4H). Our analysis revealed various perturbations upon
334 AR loss, including cells in G2/M in cluster 1 (Figure 4C). Moreover, in the fully committed cluster 3, the
335 proportion of cells in G1 dropped from ~80% in controls to ~60% in mutants, whereas those in S phase,
336 absent in control mice, increased by more than 15% in MuSC-AR deficient mice (Figure 4C), indicating
337 that they are more prone to mitotic activity.
338 To investigate the division modalities of MuSC, we performed a series of immunofluorescence
339 analyses. Double staining for PAX7 and KI67 in injured TA muscles from control and $AR^{(i)sat-/Y}$ mice at 5
340 and 7 dpi revealed a significant reduction in proliferating MuSC in mutant mice (Figures 4D-4F),
341 indicative of impaired symmetric stem cell divisions. Furthermore, double immunodetection of PAX7
342 and MYOG at 5 dpi showed a marked increase in $PAX7^+/MYOG^+$ cells, accompanied by a decrease in
343 $PAX7^+/MYOG^-$ cells upon AR loss in MuSC (Figures 4G and 4H). By 7 dpi, both $PAX7^+/MYOG^+$ and
344 $PAX7^-/MYOG^+$ cell populations exhibited a two-fold increase in $AR^{(i)sat-/Y}$ mice (Figures 4G and 4I),
345 supporting a shift from symmetric stem cell divisions toward an asymmetric division program.
346 To determine whether the absence of AR in MuSC alters their mode of division, we performed MYOG
347 and KI67 double immunostaining on injured TA muscles at 5 and 7 dpi. Notably, $MYOG^+/KI67^+$ double-
348 positive cells were detected within regenerating regions of mutant muscles (Figure 4J), consistent with
349 our scRNA-seq analysis showing an increased proportion of the committed cluster 3, characterized by
350 *Mki67* expression in mutants (Figure S4I). Quantification confirmed that $MYOG^+/KI67^+$ cells were more

351 abundant in $AR^{(i)sat-/Y}$ muscles at both 5 and 7 dpi (Figure 4K), indicating that MuSC prematurely engage
352 in the differentiation program. To further examine MuSC division behavior, single myofibers were
353 isolated from injured TA muscles at 7 dpi and analyzed *in vitro* to assess the orientation and
354 organization of satellite cell divisions. PAX7, KI67, and MYOG immunostaining revealed abnormalities
355 in $AR^{(i)sat-/Y}$ myofibers. Analysis of mitotic orientation on muscle fibers isolated from control and $AR^{(i)sat-}$
356 $^{/Y}$ mice showed perpendicular MuSC division in mutant fibers (Figure S4J), indicative of a shift toward
357 asymmetric differentiation, and suggesting disruption of the spatial control of MuSC division planes.
358 In addition, mutant fibers exhibited nuclear budding-like structures along the fiber surface, a feature
359 consistently absent in control fibers (Figure S4K). Overall, our data show that loss of AR in MuSC
360 promotes premature differentiation and alters division orientation toward asymmetric divisions.
361 We henceforth hypothesized that increased symmetric differentiation may deplete the stem cell pool,
362 compromising its ability to support effective repair during subsequent regenerative challenges. To test
363 this, we subjected control and $AR^{(i)sat-/Y}$ muscles to a secondary CTX-induced injury 28 days after the
364 primary injury, and assessed tissue morphology 7 days later (28+7 dpi). At this stage, control muscles
365 exhibited an accelerated regenerative response compared to muscles analyzed at 7 dpi following a
366 single injury (Figure 4L), consistent with previous reports [1, 32], reflecting a primed regenerative state.
367 This response was characterized by reduced immune cell infiltration (Figure 4L, cyan arrows), a
368 predominance of centrally nucleated myofibers (Figure 4L, black arrows), and minimal interstitial
369 matrix deposition (Figure 4L, green arrows). In contrast, $AR^{(i)sat-/Y}$ muscles displayed exacerbated
370 pathological features, including persistent immune infiltration (Figure 4L, cyan arrows),
371 multinucleated fibers with pronounced morphological abnormalities, and disorganized fibers with
372 fusion defects and nuclear mislocalization throughout the sarcoplasm (Figure 4L, pink arrows),
373 together with fat deposition (Figure 4L, red arrows). Immunolabeling for DMD further confirmed the
374 structural heterogeneity and irregularities in $AR^{(i)sat-/Y}$ muscles at 28+7 dpi (Figure 4M). These defects
375 were accompanied a threefold reduction in MuSC numbers in $AR^{(i)sat-/Y}$ mice compared to controls as
376 revealed by quantification PAX7-positive MuSC at 28+7 dpi (Figure 4N).
377 Overall, these results indicate that AR signaling in MuSC is essential for maintaining the stem cell pool
378 by promoting symmetric divisions and preventing premature differentiation (Figure 4O), thereby
379 ensuring effective regenerative capacity during both primary and subsequent injuries.
380
381 **AR controls MuSC fate through early chromatin remodeling**
382 To capture early AR-dependent chromatin events with the potential to drive the scRNA-seq-detected
383 transcriptomic alterations and downstream regenerative defects, we performed CUT&RUN profiling
384 of AR and the active chromatin mark H3K4me2 in young FACS-isolated MuSC at 5 dpi. Consistent with

385 our observations at 7 dpi, CUT&RUN analysis at 5 dpi identified 7,612 AR binding peaks, primarily
386 localized to intronic and intergenic regions (Figure S5A), associated with 7,040 genes. The majority of
387 these AR-bound loci coincided with H3K4me2 enrichment at promoter regions (Figures S5B and S5C).
388 Motif analysis using HOMER revealed that 50.6% of AR peaks contained canonical AR binding motifs
389 (Figure 5A), confirming the specificity of AR-DNA interactions. Functional enrichment analysis of AR
390 target genes demonstrated significant involvement in pathways critical for stem cell homeostasis and
391 tissue remodeling, notably the HIPPO and PI3K-Akt signaling pathways (Figure 5B). Similar to what we
392 described at 7 dpi, gene-centric analysis revealed that AR is mainly recruited within a 100-kb window
393 of more than 50% of differentially expressed genes (Figures 5C and 5D). Representative AR binding
394 loci at key genes involved in these regulatory pathways, including *Clock*, *Eifd2* and *Psma4*, are depicted
395 in Figure 5E. Together, these findings demonstrate that AR engages early with the MuSC chromatin
396 landscape, preferentially at distal regulatory elements enriched in active histone marks, to control the
397 transcriptional programs governing stem cell fate and tissue remodeling.
398
399 **AR dynamically repositions upon injury to govern time-dependent regenerative genomic programs**
400 The transcriptomic discrepancies observed between 5 and 7 dpi led us to question AR positioning on
401 the DNA during muscle repair. Deeptools analysis demonstrated minimal overlap and distinct peak
402 profiles for each state between AR-bound chromatin landscapes 0- (Basal), 5- and 7 dpi (Figures 5F-
403 5H). This temporal specificity was further confirmed by comparative analysis of the genes bound by
404 AR in those specific clusters (Figure 5F). The genes commonly controlled by AR during the regeneration
405 process were mainly implicated in cell-cell adhesion or in the connection with the synapse, essentially
406 *via* cadherins (e.g. *Cdh2*, *Cdh6*, *Cdh7*), and included *Ar* itself, and *Gli3* that is essential for MuSC injury
407 memory [33] (Figure 5G). More importantly, in the absence of injury, AR binding was enriched at genomic
408 loci associated with MuSC stemness, including *Pax3*, *Pax7*, and *Kdm1a* (*Lsd1*) (Figures 5G and 5H),
409 while AR-bound landscape profile markedly shifted at 5 dpi, targeting genes implicated in MuSC
410 activation, such as *Myf5* and *Tead1*, and asymmetric division like *Aurkb*, or muscle commitment
411 including *Myh4* and *Myh9* (Figures 5G and 5H). 7 dpi, AR was further reallocated to loci related to
412 myogenic differentiation such as *Myod1*, *Mef2a* and *Mef2d*, and asymmetric division like *Numb* and
413 *Pard3* (Figures 5G and 5H). Representative genes exhibiting AR binding loci in a temporal and stage-
414 specific manner during regeneration such as *Pax7*, *Myf5*, and *Myod1* are depicted in Figure 5H.
415 Collectively, these findings reveal that AR is dynamically repositioned in MuSC following injury,
416 engaging stage-specific genomic loci to orchestrate transcriptional programs that govern activation
417 and lineage commitment via MRFs (Figure 5I). This temporal chromatin remodeling ensures a

418 balanced stem-to-committed transition, safeguarding the MuSC pool for future regenerative demands
419 in young adults.
420
421 **Age-related regenerative decline in skeletal muscle is causally linked to diminished androgen**
422 **signaling**
423 Given the age-related decline in MuSC number and regenerative potential, we hypothesized that
424 diminished androgen signaling may underlie this process. We thus quantified serum testosterone
425 levels in mice at different ages and observed a progressive decrease from ~25 nmol/L in young mice
426 to a plateau of ~5 nmol/L in old ones (Figure 6A). This was accompanied by a corresponding decrease
427 in *Ar* expression at both the transcript and protein levels in non-injured (NI) TA muscle (Figures 6B-
428 6D), as well as a decrease in the number of MuSC expressing AR, compared to young mice (Figure
429 S6A). Notably, the transcript levels of the MuSC marker *Pax7* were diminished in NI TA of old control
430 mice (Figure 6E).
431 To determine the functional consequences of these baseline deficits, CTX injury was induced in 1-year-
432 old (hereafter old) control and mutant mice, derived from young mice treated with tamoxifen at 9
433 weeks and subsequently aged under natural conditions (Figure S6B). As expected, and consistent with
434 previous reports [10, 11], old male mice exhibited markedly impaired regenerative capacity compared to
435 young littermates (Figures S6C and S1K). To dissect the additional contribution of MuSC-specific AR
436 loss to this decline, we directly compared aged mutants to age-matched controls. Of note, while PAX7-
437 positive MuSC in control mice exhibited faint AR expression, it was entirely absent in $AR^{(i)sat-/Y}$ mutants
438 (Figures S6B and S6D). At 7 dpi, aged $AR^{(i)sat-/Y}$ muscles displayed increased interstitial space, sustained
439 immune infiltration, and misshaped regenerating fibers when compared to (Figure 6F). Ultrastructural
440 analysis confirmed these impairments, showing disrupted sarcomere organization, fragmented Z-
441 lines, and increased extracellular matrix deposition (Figure 6G). These structural impairments were
442 accompanied by a significant decrease in MuSC numbers (Figure 6H), and deformed regenerating
443 fibers (Figures 6I and S6E). In addition, recovery in aged muscles was accompanied by a pronounced
444 shift toward oxidative metabolism (Figure 6J), increased fibrosis (Figure 6K) and adipocyte emergence
445 (Figure 6L), highlighting the pivotal role of AR signaling in safeguarding the structural and functional
446 fidelity of regenerating muscle. Notably, the regenerative phenotype observed in aged control
447 muscles partially recapitulated features seen in young $AR^{(i)sat-/Y}$ mutants, whereas the combination of
448 aging and MuSC-specific AR loss further exacerbated these defects, highlighting the additive impact
449 of hormonal decline and receptor deficiency on regenerative capacity (Figure S6C).
450 To determine whether the regenerative impairment is causally linked to androgenic insufficiency, we
451 tested whether restoring androgen signaling could reverse aspects of the aged phenotype. We

452 thereby supplemented old mice with 5-α-dihydrotestosterone (DHT) implants. DHT supplementation
453 in old mice led to increased AR protein levels in gastrocnemius skeletal muscle 1 week after
454 implantation (Figures S6F). At 7 dpi, DHT-treated mice exhibited significantly improved muscle
455 regeneration, as evidenced by improved myofiber morphology, and an increased number of nuclei per
456 regenerating fiber (Figure 6M). Although the total number of MuSC was not significantly altered
457 (Figure 6N), we observed a slight increase in proliferating PAX7/KI67-double positive cells (Figure 6O),
458 which likely contributes to the increased number of centrally located nuclei and enhanced myogenic
459 fusion. Importantly, no significant differences were detected in differentiation capacity or immune
460 infiltration, as assessed by MYOG and F4/80 staining, respectively (Figures 6P and 6Q). In addition,
461 fibrosis analysis revealed a marked reduction in fibrotic area, with decreased collagen deposition
462 within the extracellular matrix (Figure 6R). Together, these findings provide direct evidence that age-
463 related androgen deficiency causally contributes to impaired aging skeletal muscle regeneration.
464

465 **Androgen signaling orchestrates distinct gene networks in young and old individuals leading to**
466 **similar phenotypes**

467 To understand how the age-related decline in androgen signaling affects MuSC regenerative
468 programs, we first compared the transcriptomic profiles of old control MuSC to those of young
469 counterparts at 7 dpi. This analysis identified 1,709 differentially expressed genes, including 798
470 downregulated and 911 upregulated transcripts (Figures 7A and S7A). Pathway enrichment analyses
471 of the downregulated gene set highlighted a significant suppression of pathways related to protein
472 synthesis and peptide/amide metabolism (Figure 7B), suggesting a reduced biosynthetic capacity in
473 aging MuSC. Notably, several genes essential for myogenic differentiation and structural regeneration
474 were significantly downregulated. These included *Myh4* and *Myod1* in addition to genes involved in
475 sarcomere organization and contractile function, such as nebulin (*Neb*), *Tpm3*, and troponin C type 2
476 (*Tnnc2*) (Figures 7A and 7C). This transcriptional repression is consistent with the defective
477 regenerative phenotype and histological and ultrastructural impairments observed in aged control
478 mice at 7 dpi. Conversely, pathway analyses on the 911 genes upregulated in MuSC from old control
479 mice compared to young control counterparts, revealed that these genes were predominantly
480 associated with metabolic and biosynthetic processes, notably the regulation of RNA, microRNA,
481 nitrogen metabolism, and nucleobase-containing compound metabolic pathways (Figures 7A and 7B),
482 but also oxidative metabolism processes (e.g. *Acadsb*, *Coq8b, Coq10b* and *Pdk4*) (Figures 7A and 7C),
483 collectively indicating a metabolic transition toward oxidative phosphorylation in old MuSC. These
484 molecular findings align with the histological evidence of enhanced oxidative metabolism observed at
485 7 dpi in old individuals.

486 Since aged control muscles exhibit histological and structural features reminiscent of young $AR^{(i)sat-/Y}$
487 ones, we next examined age-regulated genes to determine whether these shared changes involve AR-
488 dependent regulatory programs. To this end, we compared age-regulated genes with those
489 deregulated in young mutants and strickingly identified only 59 downregulated and 102 upregulated
490 genes common between young and aged MuSC (Figure 7D). Remarkably, a substantial fraction of
491 differentially expressed genes specific to aged MuSC exhibited AR binding within 100 kb of their TSSs
492 (Figures 7E and 7F), suggesting potential direct AR regulation. To assess the extent to which age-
493 associated transcriptional changes mimics AR loss in youth, we compared AR direct targets identified
494 in young mutant MuSC with age-regulated ones in old controls. This analysis revealed only limited
495 overlap with AR-bound genes (Figure 7G), indicating that the molecular mechanisms underlying AR
496 regulation in young MuSC differ from those driving age-associated transcriptional changes, even
497 though gene ontology analyses revealed similar functional enrichment (Figures S7D and S7F). This
498 limited convergence highlights that, while AR deficiency in MuSC at young age partially recapitulates
499 transcriptional features of aging, the molecular underpinnings differ, reflecting the distinct role of AR
500 during development as opposed to the combined decline of hormone and receptor signaling observed
501 in the elderly. Altogether, these findings support a model in which AR orchestrates regenerative
502 transcriptional programs in MuSC *via* enhancer-driven mechanisms, a regulatory framework that
503 persists with age but becomes functionally altered.
504 To extend our findings to a human model, we determined AR expression in LHCN-M2 and C79
505 myoblasts, isolated from young and aged male individuals, respectively. Notably, AR expression was
506 reduced by approximately 50% in C79 compared to LHCN-M2 myoblasts at both the transcript (Figure
507 7H) and protein levels (Figures 7I and 7J), in addition to the PAX7 levels (Figure 7K). Moreover, LHCN-
508 M2 cells displayed a higher propensity for proliferation (Figures 7L and S7I) and differentiation
509 compared to C79 cells (Figure 7M), mirroring the differences observed between young and aged mice.
510 In agreement, AR knockdown in both cell lines strongly impaired differentiation, as indicated by the
511 conservation of a fibroblast-like morphology, and lack of the characteristic spindle-shaped structure
512 observed in control cells, 5 days post-differentiation (dpd) (Figures 7M, S7J and S7K). Conversely, while
513 AR overexpression did not have flagrant effects on LHCN-M2 cells differentiation, a premature more
514 efficient myogenesis was observed in C79 cells, in the presence of elevated AR levels (Figures 7M, S7L-
515 S7N). Collectively, these findings demonstrate that intact AR signaling, requiring both sufficient ligand
516 and receptor, is essential for efficient myoblast differentiation, and by extension, effective skeletal
517 muscle regeneration.

518 **DISCUSSION**

519 Maintenance of the MuSC reservoir requires mechanisms that preserve quiescence, while ensuring
520 that repair proceeds with structural and functional fidelity. In young male skeletal muscle, AR
521 expression concentrates in the most quiescent, self-renewing MuSC states, and is largely extinguished
522 as cells commit. Conditional loss of AR in MuSC disrupts dormancy, accelerates cell-cycle entry, and
523 drives symmetric differentiation on the expense of stem cells renewal, leading to attrition of the
524 regenerative pool. Notably, bulk RNA-seq at 7 dpi reveals significant impairments in *Pax7*, *Myf5*,
525 *Myod1*, *Myog*, and *Mymx* expression in $AR^{(i)sat^{-}/Y}$ cells, whereas scRNA-seq at 5 dpi does not detect
526 these changes. This discrepancy reflects differences in both regeneration stage and analytical
527 resolution as bulk RNA-seq captures population-wide transcriptional shifts later in repair, whereas
528 scRNA-seq interrogates cell-state-specific signatures at an earlier time point, without implying a
529 biological inconsistency. On this basis, we here identify AR as lineage-intrinsic indicator of MuSC
530 stemness in males, functionally distinct from its canonical anabolic role in myofibers [16, 25, 26, 34].

531 This AR-stemness relationship fits within a broader endocrine framework across the male life course.
532 At young age, androgens promote the establishment of a long-lived quiescent MuSC pool from
533 juvenile precursors through a Notch-dependent pathway [18]. With aging, declining systemic androgens
534 correlate with reduced MuSC number and impaired repair [35], and androgen supplementation restores
535 regenerative capacity in low-androgen settings [36, 37]. Consistent with this trajectory, our MuSC-specific
536 AR knockout phenotypically recapitulates features of aging-associated stem cell exhaustion, including
537 reduced responsiveness to repeated injuries, suggesting that androgen decline and diminished AR
538 activity converge on shared mechanisms that erode the MuSC reservoir. It is worth noting, however,
539 that transcriptomic differences observed between AR-deficient young MuSC and those from aged
540 controls may also reflect distinct underlying causes, namely, the selective inactivation of AR in
541 otherwise intact young MuSC versus the broader loss of stem cells with age, along with age-related
542 alterations in the muscle microenvironment [38]. These observations indicate that androgen decline and
543 AR loss exert distinct yet complementary effects, the former reduces stem cell abundance and
544 responsiveness, while the latter disrupts intrinsic programs of quiescence and fate. In aged AR-
545 deficient mutants, these deficits appear to sum, producing an exacerbated phenotype that
546 underscores the dual contribution of hormone and receptor to MuSC maintenance.

547 We also observe that AR expression in young individuals persists for weeks after injury in MuSC
548 derived from self-renewal, reflecting early symmetric divisions driven by AR that maintain the
549 quiescent stem pool for future regenerative demands. In contrast, differentiating MuSC gradually lose
550 AR, showing that AR not only supports stem cell expansion, but also controls asymmetric divisions to
551 produce committed cells for repair. Without AR, MuSC divisions favor committed daughters over self-

552 renewal, depleting the reserve and impairing regeneration after repeated injury. This AR-dependent
553 balance between renewal and differentiation in male MuSC has not been shown *in vivo* before. Earlier
554 studies using female-derived C2C12 myoblasts showed DHT enhances proliferation, but these cells
555 lack true quiescence and do not represent adult male muscle stem cells [20, 42, 43]. In contrast, our findings
556 reveal that physiological androgen levels *via* AR in male MuSC dynamically regulates their fate during
557 regeneration.
558 MuSC-AR influences more than lineage fate in skeletal muscle. It promotes proliferation and
559 differentiation in myogenic cells [44, 45], and its loss in our mouse model leads to fusion defects, fiber
560 orientation defaults, and impaired ultrastructure, reflecting not only reduced progenitor output, but
561 also a disrupted regenerative program in these progenitors. This contradicts earlier claims that MuSC-
562 AR is dispensable for regeneration (Sakai et al., 2020), likely because their model did not disrupt AR in
563 the early, true stem MuSC population. Our data clearly establish MuSC-intrinsic AR as a crucial
564 regulator of androgen-driven muscle repair in males. This signaling axis also shapes metabolic identity.
565 While myofiber-AR supports glycolytic metabolism, its absence in MuSC at young age shifts
566 regenerated fibers toward oxidative pathways, which was recapitulated in aged individuals. Seahorse
567 assays and histology confirm this shift, consistent with findings in AR-deficient myofibers [25, 46], AR-
568 related disorders [47], and aging muscle [48, 49]. Notably, myofiber-AR loss is linked to increased β-oxidation
569 gene expression and reduced Complex IV components [25, 50], though this latter feature was absent in
570 our model, possibly due to reactive oxygen species accumulation impairing electron transport and
571 causing mitochondrial stress [51].
572 At the tissue level, MuSC-AR deletion in young individuals reveals increased inflammation, fibrosis,
573 and adipocyte accumulation at the site of injury. Similar disturbances occur in androgen-deprived
574 states, where impaired inflammatory resolution and accelerated fibro-adipogenic drift are observed
575 [52, 53]. These findings show that MuSC are not passive recipients, but active transmitters of androgen-
576 sensitive signals shaping their microenvironment. This supports a bidirectional model in which AR in
577 MuSC governs intrinsic fate decisions while orchestrating stromal and immune crosstalk during muscle
578 repair. While our data indicate that MuSC-AR influences macrophages and FAPs, these effects are
579 likely indirect. CellChat analysis did not reveal significant differences in secreted signaling molecules,
580 and *in vitro* co-culture experiments were precluded by the poor adherence of FACS-isolated $AR^{(i)sat^{-}/Y}$
581 MuSC. Therefore, MuSC-AR appears to shape the regenerative niche predominantly through indirect
582 intercellular mechanisms. Importantly, in AR-deficient muscles, macrophages prematurely express
583 anti-inflammatory markers, yet the total inflammatory burden persists longer, reflecting an
584 uncoupling between phenotypic transition and effective clearance. This aberrant trajectory likely
585 contributes to impaired regeneration and highlights the nuanced role of MuSC-AR in coordinating the

586 immune niche. Our CellChat analysis further suggests that AR-deficient MuSC perturb intercellular
587 communication with macrophages and FAPs, although the precise signaling mediators remain to be
588 defined. Identifying these factors represents a compelling avenue for future work, as it would
589 illuminate the mechanisms by which MuSC orchestrate niche remodeling and coordinate
590 regeneration.
591 To coordinate these diverse, stage-specific functions during muscle regeneration, we propose a
592 dynamic chromatin occupancy model in which AR sequentially engages distinct transcriptional
593 programs as MuSC progress from quiescence through activation to commitment. Such nuclear
594 receptor mobility and partner switching are well documented in other systems [54-57]. Emerging
595 evidence in skeletal muscle shows AR collaborates with SMAD signaling to enhance BMP-driven
596 transcriptional programs that regulate muscle mass and quality [58]. In aging and pathological
597 expansions of the AR-polyglutamine tract, altered chromatin binding and disrupted co-factor
598 interactions have been observed [59, 60], suggesting that reduced AR availability with age may limit its
599 genomic sampling and assembly of stage-specific complexes necessary to maintain stemness, and
600 sequentially enable differentiation.
601 In sum, MuSC-AR preserves quiescence, sustains the stem cell pool, shapes glycolytic identity, and
602 orchestrates niche remodeling. Its decline leads to reserve loss, metabolic drift, and regenerative
603 failure (Figure S7O), highlighting MuSC-AR as a therapeutic target in aging and disease.
604

605 **METHODS**

606 **Mouse Studies**

607 ***Housing***

608 Mice were maintained on a C57BL/6 background and housed in a temperature- and humidity-
609 controlled facility under a 12-hour light/dark cycle, with *ad libitum* access to standard rodent chow
610 (2800 kcal/kg, Usine d'Alimentation Rationelle, Villemoisson-sur-Orge, France) and water. Breeding
611 and maintenance followed institutional guidelines, and all experiments were conducted in an
612 accredited facility in compliance with French and EU regulations on laboratory animal use (Directive
613 2010/63/EU). Procedures were approved by the local ethical committee (Com'Eth, Strasbourg, France)
614 and by the French Ministry of Research (MESR). Mice were euthanized *via* cervical dislocation, and
615 muscles were harvested for histological and molecular analysis.

616

617 ***Generation of AR$^{(i)sat-/Y}$ mutant mice***

618 For satellite cell-specific androgen receptor (AR) ablation, AR$^{L2/L2}$ female mice, carrying LoxP sites
619 flanking chromosome X exon 1 encoding the AR N-terminal domain [61], were intercrossed with *Pax7*-
620 CreER^{T2} male mice [62] to generate *Pax7*-CreER^{T2}/AR$^{L2/Y}$ mice, which express CreER^{T2} recombinase
621 selectively in satellite cells. To induce recombination, 9-week-old AR$^{L2/Y}$ control males and their *Pax7*-
622 CreER^{T2}/AR$^{L2/Y}$ pre-mutant littermates received intraperitoneal tamoxifen injections (1
623 mg/mouse/day) for five consecutive days, generating control and AR$^{(i)sat-/Y}$ mutant mice. Alternatively,
624 mice were intercrossed with a *Rosa26*-YFP reporter line [63] to generate *Pax7*-CreER^{T2}/AR$^{L2/Y}$/*Rosa26*-
625 YFP$^{Tg/0}$ mice with one YFP allele, allowing selective labeling of satellite cells and lineage tracing of their
626 progeny. *Pax7*-CreER^{T2}/Rosa26-YFP$^{Tg/0}$ mice lacking the floxed AR allele were used as additional
627 controls. Mice were analyzed at 3 months of age (young adults) or at 1 year of age (aged cohort).
628 Primer sequences required for genotyping PCR are listed in Table S4.

629

630 ***Mouse Treatments***

631 For cardiotoxin-induced muscle injury model, 3 months young adults or at 1-year aged mice were
632 anesthetized with 2.5% isoflurane using a SomnoSuite device. To induce muscle damage, 20 µl of
633 25 µM cardiotoxin (CTX) (Latoxan, Valence, France, L8102), dissolved in phosphate-buffered saline
634 (PBS) were injected into the tibialis anterior (TA) muscle.

635 For androgen supplementation, 5-alpha-dehydrotestosterone (DHT) implants were inserted
636 subcutaneously in the intrascapular region of 21-month-old wild-type male mice, as described [64].
637 Muscle injury was induced by CTX injection three weeks post-implantation to avoid off-target effects
638 caused by DHT-burst.

639 **Testosterone serum levels measurement**

640 Blood was collected from mice in 50 mM EDTA tubes (Sigma-Aldrich), and plasma was isolated by
641 centrifugation at 3,000 g for 15 minutes at 4°C. The supernatant was collected, and serum
642 testosterone levels were quantified using the Testosterone Rat/Mouse ELISA Kit (LDN, AR E-8000R),
643 following the manufacturer's instructions.

644

645 **Contractile Measurements**

646 *In situ* isometric TA muscle force in response to nerve stimulation was measured as described [26]. In
647 brief, specific maximal tetanic force (mN/mm^2) was determined by dividing the measured force by the
648 estimated CSA of the muscle. Assuming a cylindrical muscle shape with a density of 1.06 mg/mm^3, the
649 CSA was calculated as the volume of the muscle divided by its (muscle) length. The optimal muscle
650 length (L0) was defined as the length at which maximal tetanic force was observed. All data collected
651 from the muscle lever system were recorded and analyzed using a microcomputer with the
652 PowerLab/4SP system (AD Instruments).

653

654 **Histological analyses**

655 ***Muscle histology***

656 Muscles were either snap-frozen in liquid nitrogen-cooled isopentane for cryosections, or fixed in 4%
657 PFA overnight at 4 °C then washed in PBS and 70% ethanol and embedded in paraffin. 10 µm thick
658 cryosections were prepared at −20 °C using a 2800 Frigocut cryostat (Leica, St Jouarre, France) and
659 kept at −20 °C until further analysis. 5 µm thick paraffin sections were cut at room temperature (RT)
660 using a microtome (Leica RM, 2145, 0737/09.1998) and stored at 4 °C until further analysis.
661 Hematoxylin and eosin, and Masson's Trichrome staining were performed on paraffin sections as
662 described, while NADH and COX staining were assessed on cryo-sections as described [25, 63, 65].

663

664 ***Quantification of Collagen Deposition***

665 Collagen content assessed by Sirius Red staining (Picro-Sirius Red Stain, Pint, StatLab, STPSRPT) was
666 imaged under a bright-field microscope, or under polarized light using the Axioscan 7 (Carl Zeiss) slide
667 scanner. Birefringent collagen fibers were visualized based on their differential light refraction
668 properties, allowing for the selective detection of collagen deposition. Quantification was performed
669 by analyzing the polarized signal intensity and distribution across the tissue using standardized image
670 analysis parameters established by the in-house anatomic pathology platform.

671

672

673 ***Immunofluorescence staining***

674 Paraffin and cryo-sections were processed using distinct protocols tailored to antibody requirements.
675 Paraffin sections underwent deparaffinization, and antigen retrieval was done under controlled
676 temperature and pressure conditions for 20 min in either tris-hydroxymethyl-aminomethane (Tris
677 buffer) (pH=9.0) or in Signal Stain ® Citrate Unmasking Solution (Cell Signalling 14746S). In contrast,
678 frozen sections were fixed for 10 min in 4% PFA at RT, and permeabilized with PBST for 15 min at RT.
679 Afterwards, paraffin or frozen sections were incubated overnight at 4 °C with the primary antibodies
680 diluted in PBST directed against AR (Rabbit, Abcam, ab108341, 1:500), PAX7 (Rabbit; Thermo Fisher,
681 PA1-117, 1:400, or Mouse; DSHB, AB_528428, 1:50), MYOG (Abcam, ab1835, 1:400), ACTN1 (Mouse,
682 Abcam, ab9465, 1:400), DMD (Mouse, IGBMC , 1Dystro1D2, 1:1000 or Rabbit sigma, D8168, 1:400),
683 KI67 (Rat, R&D systems, 14-5698-82, 1:500), LAMA2 (Rat, Sigma Aldrich, L0663-.1ML, 1:500), eMyHC
684 (Mouse, DSHB, F1.652, 1:20), F4/80 (Rabbit, Cell Signaling, 70076, 1:400) and PLIN1 (Rabbit, Abcam,
685 Ab3526. 1:200). Mouse (Santa Cruz Biotechnology, E3117, 1:500), rat (Vector Laboratories, BA-4000,
686 1:500) or rabbit (PeproTech, 500-P000-500UG, 1:500). IgGs were used as controls. Sections were
687 rinsed with wash buffer, and incubated with appropriate Alexa-Fluor-conjugated secondary antibodies
688 with different fluorescent wavelengths (488, 555 or 647 nm, 1:500, Invitrogen: a32732, a32723,
689 a21206, a21424, a48265, a32733, a32728) in permeabilization buffer for 45 min at RT. After wash,
690 slides were mounted with Fluoromount™ Aqueous Mounting medium containing DAPI (Invitrogen,
691 00-4959-52).

692

693 ***Fiber cross-sectional area measurements***

694 Muscle cross-sections were stained with DMD (Abcam, ab15277, 1:500) mark the sarcolemma
695 surrounding each fiber. CSAs were quantified using QuPath (open-source image analysis software)
696 integrated with a customized Groovy macro (available via GitLab). In brief, individual fibers were
697 identified based on the intensity and continuity of the stained sarcolemma surrounding each fiber by
698 segmentation. Areas were measured after background subtraction and automated thresholding.

699

700 ***Quantification of F4/80 and CD163 mean fluorescence intensity (MFI)***

701 Fluorescence images of injured TA muscles immunostained for F4/80 and CD163 were analyzed using
702 QuPath software (QuPath-0.5.0). Regions of interest (ROIs) corresponding to the injured areas were
703 annotated manually, and a pixel classifier was trained on these annotations to categorize pixels as
704 background/negative, positive signal, or other non-positive signals. Fluorescence intensity thresholds
705 were set manually for each marker to ensure accurate detection of positive staining. Mean

706 fluorescence intensity within the annotated ROIs was then measured and exported for further
707 analysis.
708
709 ***Muscle ultrastructural analysis***
710 1 mm² TA muscle samples were fixed overnight at 4°C by immersion in a mix of 2.5% glutaraldehyde
711 and 2.5% paraformaldehyde diluted in 0.1 M cacodylate buffer (pH 7.4), washed in the same buffer
712 for 30 min, and stored at 4°C. Post-fixation was performed with 1% osmium tetroxide in 0.1 M
713 cacodylate buffer for 1 h at 4°C, followed by dehydration through a graded ethanol series (50%, 70%,
714 90%, and 100%) and propylene oxide (30 min each). Samples were oriented longitudinally or
715 transversally and embedded in Epon 812. 70 nm ultrathin sections were obtained and contrasted with
716 uranyl acetate and lead citrate. Imaging was performed at 70 kV using a Morgagni 268D electron
717 microscope, with digital acquisition via a Mega View III camera (Soft Imaging System).
718
719 **Cell culture analyses**
720 ***Cell culture and treatments***
721 LHCN-M2 and C79 cells were cultured in Dulbecco's Modified Eagle Medium (DMEM 4,5 g/L of glucose,
722 Invitrogen 4165-062)/Medium 199 (Invitrogen 22340-020) (4:1), supplemented with 20% fetal calf
723 serum (FCS), 25 µg/mL fetuin, 5 µg/mL human insulin, 40 µg/mL gentamycin and 0.5 ng/mL basic
724 fibroblast growth factor (bFGF) along with 5 ng/mL human epidermal growth factor (hEGF) and 0.2
725 µg/mL dexamethasone [66]. Cells were maintained at 37°C in a humidified atmosphere with 5% CO_2.
726 Cells were split at 70-80% confluence, and the medium was replaced every 48 hours.
727 To induce differentiation, LHCN-M2 and C79 cells were seeded at 90% confluence and switched at
728 confluence to differentiation medium (DMEM supplemented with 2% horse serum and 40 µg/mL
729 gentamycin) for up to 5 days, with medium changes every 48 hours.
730 For transfection, human AR siRNA (5'-GGGCACTTCGACCATTTCTGA-3'), or scramble siRNA (5'-
731 AAGCTTCATAAGGCGCATAGC-3'), were introduced using Typical RNAiMAX Transfection kit
732 (ThermoFischer, 13778075), following the manufacturer's protocol. Cells were seeded in six-well plate
733 and transfected with 50 nM siRNA diluted in Opti-MEM (Gibco, USA) at 50-60% confluence for 24h,
734 after which the medium was replaced with fresh differentiation or growth medium. Cells were
735 subsequently treated with 100 nM of DHT (Sigma, A8380-1G) diluted in ethanol 24h after
736 transfections.
737 For AR overexpression, MuSC were transfected with the pEGFP-AR^{WT} plasmid using Lipofectamine
738 2000 DNA Transfection kit (ThermoFisher, 11668027), according to the manufacturer's instructions.
739 Cells were seeded in six-well plate and transfected with 14 µg pEGFP-AR^{WT} plasmid diluted in Opti-

740 MEM (Gibco, USA) at 50-60% confluence for 24h, after which the medium was replaced with fresh
741 differentiation or growth medium. Cells were subsequently treated with 100 nM of DHT (Sigma,
742 A8380-1G) diluted in ethanol 24h after transfections.
743
744 ***Cell Proliferation Analysis***
745 Cell proliferation was assessed using the CellTrace™ CFSE (Carboxyfluorescein Succinimidyl Ester)
746 Assay (Thermo Fisher Scientific, USA, C34557) as described [67]. Briefly, LHCN-M2 and C79 cells were
747 incubated with 5 µM CFSE at 37°C for 20 min in a humidified atmosphere with 5% CO_2. The labeling
748 reaction was quenched by adding an equal volume of complete growth medium, followed by two
749 washes with PBS to remove excess dye. Labeled cells were kept in appropriate culture conditions and
750 collected at 24-, 48-, and 72-hours post-labeling for flow cytometry analysis. CFSE fluorescence
751 intensity was measured using a flow cytometer (BD LSRFortessa™, BD Biosciences, USA) with
752 excitation at 488 nm and emission detection at 530 nm. Data were analyzed using FlowJo software
753 (BD Biosciences, USA), and cell proliferation was determined by monitoring the progressive dilution
754 of CFSE fluorescence across multiple cell generations. To identify non- and slow-proliferating cells, we
755 defined the 30% of cells exhibiting the highest CellTrace Violet signal in control as the reference
756 population, and calculated the proportion of cells with equal or greater signal intensity.
757
758 ***Immunocytochemistry***
759 Immunocytofluorescence assay was performed by incubating fixed LHCN-M2 and C79 cells with AR
760 (Rabbit, Abcam, ab108341, 1:500) and PAX7 (Mouse; DSHB, AB_528428, 1:50) antibodies.
761 Observations were made under a Leica confocal microscope.
762
763 ***Seahorse analysis of LHCN-M2 myoblasts***
764 Mitochondrial respiration was assessed using the Seahorse XF Cell Mito Stress Test Kit (Agilent
765 Technologies, Part Number: 103015-100) according to the manufacturer's protocol. Briefly, ~1800
766 LHCN-M2 myoblasts were seeded in Seahorse XF cell culture microplates (Agilent), and treated with
767 either vehicle or 100 nM flutamide (Abcam, ab141234) for 1 hour. The assay was performed on a
768 Seahorse XFe96 Analyzer (Agilent), following the sequential injection of oligomycin (1 µM), FCCP (2.5
769 µM), and rotenone/antimycin A (1 µM). Basal respiration, ATP-linked respiration, maximal respiration,
770 and spare respiratory capacity were calculated using Wave software (Agilent).
771
772
773

774 **Flow cytometry analysis**

775 ***Muscle cell populations composition***

776 Muscle stromal vascular fraction was isolated as described [68]. Briefly, hind limb muscles were
777 dissected, minced into small fragments, and enzymatically digested with 1.25 U/mL Dispase II
778 (Stemcell Technologies, Cat: 07913) and 500 µg/mL Collagenase Type I (Thermo Fisher Scientific,
779 17018029). The resulting cell suspension was sequentially filtered through 100 µm, 70 µm, and 40 µm
780 cell strainers (Corning Life Sciences) to remove debris. Cells isolated from digested muscle tissue were
781 stained with CD45 Alexa eFluor700 (eBioscience, 56-0451-82, 1:100), CD31 PE (eBioscience, 12-0311-
782 82, 1:100), SCA-1 PE-Cy7 (eBioscience, 25-5981-82, 1:100), and Integrin-α7 (ITGA7) FITC (MBL, K0046-
783 4, 1:50). Cells were analyzed based on forward scatter (FSC) and side scatter (SSC) parameters to
784 exclude debris and doublets. CD45- and CD31-positive cells were quantified to assess immune and
785 endothelial cell populations, respectively. After removing CD45/CD31-expressing cells, SCA-1-positive
786 cells were gated to identify fibro-adipogenic progenitor cells (FAPs). Finally, SCA-1-negative, ITGA7-
787 positive cells were classified as satellite cells. Fluorescence intensity was measured using a flow
788 cytometer (BD FACSymphony A1™, BD Biosciences, USA). Analysis were conducted using FlowJO
789 software as described [68].

790

791 ***Muscle immune cell populations composition***

792 Cells isolated from digested muscle tissue were stained with CD45 Alexa eFluor700 (eBioscience, 56-
793 0451-82, 1:100), CD11b PerCP-Cy5.5 (BioLegend, 101228, 1:100), Ly-6G-GR-1 FITC 488 (BioLegend,
794 108417, 1:100), Ly-6C PE-CF594 (BD Horizon™, AB_2737749, 1:100), and F4/80 APC eFluor 780
795 (eBioscience™, 47-4801-82, 1:100). Cells were analyzed based on forward scatter (FSC) and side
796 scatter (SSC) parameters to exclude debris and doublets.

797 Data analysis was performed by sequential gating on single, live $CD45^+$ leukocytes, followed by
798 identification of myeloid cells as $CD11b^+$, neutrophils as $CD11b^+Ly6G^+$, monocytes as
799 $CD11b^+Ly6G^-Ly6C^+$, and macrophages as $CD11b^+Ly6G^-$ $Ly6C^-F4/80^+$. Fluorescence intensity was
800 measured using a flow cytometer (BD FACSymphony A1™, BD Biosciences, USA). Analyses were
801 conducted using FlowJO software.

802

803 **Fluorescence-Activated Cell Sorting (FACS) of Satellite Cells**

804 After stromal vascular fraction isolation, mononucleated cells were pelleted by centrifugation at 400g
805 for 5 min, resuspended in FACS buffer (DMEM without phenol red, 4.5 g/L glucose, 2% BSA, 2 mM
806 EDTA), and labeled with fluorescence-conjugated antibodies. Cells were stained with CD45 PE
807 (eBioscience, 12-0451-83, 1:100), CD11b PE-Cy7 (eBioscience, 25-0112-82, 1:100), CD31 PE

808 (eBioscience, 12-0311-82, 1:100), TER119 PE (BD Pharmingen™, 553673, 1:100), ITGA7 FITC (MBL,
809 K0046-4, 1:50), CXCR4 APC (eBioscience, 17-9991-82, 1:100), and CD34 eFluor405 (eBioscience, 48-
810 0341-82, 1:33). Cells were gated based on FSC and SSC parameters to exclude cellular debris and
811 doublets. Leukocytes and endothelial cells were removed by gating out CD45-, CD11b-, CD31-, and
812 TER119-positive populations. The remaining fraction was further gated for CD34 and ITGA7
813 expression, and double-positive cells were selected based on CXCR4 expression. Fluorescence
814 intensity and sorting were conducted using a FACS sorter (BD FACSAria™, BD Biosciences, USA). Sorted
815 satellite cells were subsequently processed for RNA extraction or CUT&RUN analyses.
816
817 **CUT&RUN Assay and Bioinformatics Analysis**
818 CUT&RUN was performed as described [68, 69]. Briefly, FACS-isolated satellite cells were centrifuged at
819 500 g for 10 min at 4°C, and the resulting cell pellet was incubated with nuclear extraction buffer
820 (20mM HEPES-KOH pH = 7.9, 10 mM KCl, 0.5 mM Spermidine, 0.1% Triton X-100, 20% Glycerol and
821 protease inhibitor cocktail) for 20 min on ice. Isolated nuclei were then washed and incubated with
822 Concanavalin A-coated beads (BioMag Plus Concanavalin A, Cat: 86057-3) for 10 min at 4°C. Following
823 additional washes, the nuclei-bead complexes were incubated overnight at 4°C with gentle agitation
824 in the presence of primary antibodies targeting AR (Abcam, ab108341, 1:100) and H3K4me2 (Active
825 Motif, 39141, 1:100), and a Rabbit IgG (PeproTech, 500-P000-500UG, 1:100). Nuclei-bead complexes
826 were precipitated and incubated with protein A-micrococcal nuclease (pA-MN, IGBMC) for 1 h at 4°C
827 under constant agitation. Enzymatic cleavage was initiated by adding 3 µL of 100 mM $CaCl_2$, followed
828 by 30 min of incubation on ice. The reaction was terminated at 37°C for 20 min using stop buffer (200
829 mM NaCl, 20 mM EDTA, 4 mM EGTA, 50 µg/mL RNase A, 40 µg/mL glycogen, 25 pg/mL yeast spike-in
830 DNA). DNA was extracted from immunoprecipitated samples for sequencing.
831 Libraries were generated from immunoprecipitated DNA as described [68], and sequenced on an
832 Illumina HiSeq 2000 platform. Reads overlapping ENCODE blacklist regions (V2) were removed, and
833 deduplicated unique reads were conserved for further analysis. Reads were mapped to the mm10
834 reference genome using Bowtie2 (v2.3.4.3) [70]. To generate genome-wide intensity profiles, uniquely
835 mapped reads were processed as follows: Bigwig files were generated using bamCoverage (deeptools
836 3.3.0) [71], with normalization by RPKM (--normalizeUsing RPKM --binSize 20). Raw bedgraph files were
837 produced with genomeCoverageBed (bedtools v2.26.0) [72]. Peak calling was performed using SEACR [73]
838 and MACS2 [74] with IgG-immunoprecipitated samples as controls (-keepall), and peaks with an FDR at
839 least less than 0.05 were retained for further analysis. The IGV genome browser
840 (http://software.broadinstitute.org/software/igv/) was used for genome-wide intensity visualization.
841 Peaks were annotated, and motif analysis was conducted using HOMER. Genomic feature distribution

842 (promoters/TSS, 5' UTRs, exons, introns, 3' UTRs, transcription termination sites, and intergenic
843 regions) was determined based on RefSeq and HOMER annotations. For bioinformatics and clustering
844 analysis, Venn diagrams were generated using Venny (2.1.0)
845 (https://bioinfogp.cnb.csic.es/tools/venny/).
846 Clustering analyses were performed using seqMINER [75] and deeptools (-computeMatrix -skip0; -
847 plotHeatmap) with K-Means linear normalization. Genomic intersections and sequence extractions
848 were carried out using bedtools. GetFastaBed was used to extract FASTA sequences from BED files.
849 Intersect Interval and Multiple Intersect were applied to identify overlapping genomic locations.
850 WindowBed was utilized for gene-centric peak distribution analyses. When not specified, all
851 bioinformatics analyses were performed using default parameters, ensuring robust and reproducible
852 results.
853
854 **RNA extraction and analyses**
855 Total RNA from muscle tissue, LHCN-M2 and C79 cell lines was extracted using TRIzol reagent
856 (TRIREAGENT, Molecular Research Center, TR-118, 513-841-0900) as described [76]. RNA concentration
857 and purity were assessed spectrophotometrically using a NanoDrop system (Thermo Fisher Scientific).
858 For RNA isolation from FACS-isolated MuSC, the RNeasy Plus Micro Kit (Qiagen, 74034) was employed
859 according to the manufacturer's instructions.
860 For RT-qPCR experiments, 2 µg of total RNA underwent reverse transcription using SuperScript IV (Life
861 Technologies) with oligo(dT) primers, according to the supplier's protocol. cDNA was diluted hundred
862 times and quantitative PCR (qPCR) was performed with a Lightcycler 480 II (Roche) using the SYBR®
863 Green PCR kit (Roche), in accordance with the recommended protocol (2 µl cDNA, 4.8 µl H_2O, 5 µl
864 Syber Green 2x mix and 0.2 µl of 100 µM primer mix). The primer sequences for mouse and human
865 are detailed in Tables S5 and S6, respectively. Housekeeping genes *Tbp* (for mouse), and *HSP90AB1*
866 (for human) were used as internal controls. Data were analyzed using ΔΔCt [77] method.
867 For RNA sequencing (RNA-seq) and SMART-seq experiments, RNA integrity was assessed using a
868 Bioanalyzer. Library preparation was performed at the GenomEast platform from IGBMC.
869 For RNA-seq, cDNA library was prepared, and sequenced by the standard Illumina protocol (HiSeq
870 4000, single-end, 50 bp), following the manufacturer's instructions. Image analysis and base calling
871 were performed using RTA 2.7.7 and bcl2fastq 2.17.1.14. Adapter dimer reads were removed using
872 DimerRemover. FastQC 0.11.2 (http://www.bioinformatics.babraham.ac.uk/projects/fastqc/) was
873 used to evaluate the quality of the sequencing. Reads were mapped to the mouse mm10 genome
874 (NCBI Build 38) using STAR v2.7.10b [78]. Only uniquely aligned reads were retained for further analyses.

875 Quantification of gene expression was performed using HTSeq 0.11.0 [79]. For comparison among
876 datasets, the transcripts with more than 100 raw reads were considered.
877 For SMART-seq, full length cDNA was generated from 250 pg to 2 ng of total RNA using SMART-Seq®
878 mRNA Kit (Takara Bio Europe, Saint Germain en Laye, France), according to manufacturer's
879 instructions, with 12 cycles of PCR for cDNA amplification by Seq-Amp polymerase. Six hundred pg of
880 pre-amplified cDNA were used as input for Tn5 transposon tagmentation followed by 12 cycles of
881 library amplification using Nextera XT DNA Library Preparation Kit and IDT for Illumina DNA/RNA UD
882 Indexes, Tagmentation (Illumina, San Diego, USA). Following purification with SPRIselect beads
883 (Beckman-Coulter, Villepinte, France), the size and concentration of libraries were assessed using
884 Bioanalyzer 2100 system (Agilent technologies, Les Ulis, France). Libraries were sequenced on an
885 Illumina NextSeq 2000-X sequencer as paired-end 50 base reads. Image analysis and base calling were
886 performed using RTA version 2.7.7 and BCL Convert version 3.8.4. Adapter dimer reads were removed
887 with DimerRemover (-a AGATCGGAAGAGCACACGTCTGAACTCCAGTCAC), and the quality of
888 sequencing data was evaluated using FastQC 0.11.5. Reads were aligned to the mouse mm39 genome
889 using STAR v2.7.10b, retaining only uniquely mapped reads for downstream analyses. Gene expression
890 was quantified using STAR, and for dataset comparisons, only transcripts with more than 50 raw reads
891 were considered.
892 For RNA sequencing (RNA-seq) and SMART-seq experiments, differentially expressed genes (DEGs)
893 were identified using the Bioconductor libraries DESeq2 [80] with a $p < 0.05$. Identified DEGs were
894 subjected to functional analysis using STRING 12.0 [81] and to pathway analysis using WebGestalt [82] with
895 the Over-Representation Analysis (ORA) method, applying a false discovery rate (FDR) < 0.05 as the
896 significance threshold. Heatmaps were generated by centering and normalizing expression values
897 using Cluster 3.0 [83], with subsequent visualization Morpheus
898 (https://software.broadinstitute.org/morpheus/). Genes were clustered using K-Mean with gene tree
899 construction, Pearson correlation, and average linkage as clustering parameters [84].
900
901 **Single-cell RNA sequencing**
902 Single-cell RNA sequencing (scRNA-seq) experiments were performed on TA muscle cells, isolated
903 from 3 control ($AR^{L2/Y}$) and 3 $AR^{(i)sat-/Y}/YFP^{Tg/0}$ injured TA muscles at 5 dpi. TA muscles were dissociated
904 into single cells, as described above. Cells from each genotype group were pooled and stained with
905 DAPI, and DAPI-negative living cells were isolated using a BD FACS Aria™ Fusion flow cytometer. To
906 assess cell viability and yield, a Trypan blue exclusion assay was performed using a Neubauer Chamber.
907 Only samples with a viability greater than 95% were processed using a Chromium Controller (10X
908 Genomics, Leiden, The Netherlands). 16,500 total cells were loaded per well to yield approximately

909 10,000 captured cells into nanoliter-scale Gel Beads-in-Emulsion (GEMs). Single cell 3 prime mRNA seq
910 library were generated using Chromium Next GEM Single Cell 3 prime Reagent Kits v3.1 (10X
911 Genomics). Libraries were quantified and controlled for their quality using Bioanalyzer 2100 (Agilent
912 Technologies, Santa Clara CA), and further sequenced on an Illumina NextSeq 550 sequencer as
913 paired-end 28 + 100 base reads. Image analysis and base calling were performed using RTA version
914 2.7.7 [85] and Cell Ranger version 3.0.2 [86].
915 Data were processed using the Cell Ranger 7.0.0 count pipeline (10x Genomics) for read alignment,
916 barcode and unique molecular identifier (UMI) filtering, and gene quantification. A custom reference
917 genome was generated using the mkref function with the GRCm39 assembly of the *Mus musculus*
918 genome and Ensembl release 107 annotations. The output gene-barcode matrix was imported into
919 RStudio (version 2025.05.1) using the Read10X function from the Seurat package (version 5), yielding
920 a sparse matrix of UMI counts per gene per cell. Downstream analyses were conducted in RStudio
921 following standard Seurat v5 workflows [87], including quality control, normalization, dimensionality
922 reduction, clustering, and differential gene expression. For quality control, cells with <10%
923 mitochondrial content, <50% ribosomal gene expression, and total RNA features between 200 and
924 6000 were retained. Principal Component Analysis (PCA, dim=16) was used for dimensionality
925 reduction, and clustering was performed using a resolution parameter of 0.6. Differential gene
926 expression and further downstream analyses were conducted. Satellite cell reclustering was
927 performed with dimension reduction of 14 and cluster resolution of 0.3.
928 Cell-cell communication analysis was conducted using the CellChat R package within the RStudio
929 environment [88]. Normalized scRNA-seq data were used, and overexpressed ligands and receptors
930 were identified to infer intercellular signaling networks. Communication probabilities were computed
931 using the trimean method, with a minimum gene expression threshold of 0.1, and genes were
932 considered only if expressed in more than 10% of cells in the described groups. The CellChatDB ligand-
933 receptor interaction database was used as the reference. The analysis pipeline included identification
934 of major signaling inputs and outputs, classification of signaling roles (incoming, outgoing, mediator,
935 and influencer), and visualization via circle plots and hierarchical clustering. Inter-condition
936 comparisons were performed using the compareInteractions and rankNet functions. All analyses were
937 performed using default CellChat parameters, including 500 permutations for significance testing and
938 standard visualization settings, unless otherwise specified. Results were visualized and further
939 interpreted using built-in and custom R scripts. Cell cycle bioinformatic analyses were performed using
940 Scanpy function (scanpy.tl.score_genes_cell_cycle), with marker genes extracted from scRNA-seq of
941 mouse embryonic stem cells generated for DeepCycle as described [87, 89].
942

943 **Protein analysis**

944 TA muscles were mechanically ground in RIPA buffer [50 mM Tris (pH 7.5), 1% NP-40, 0.5% sodium
945 deoxycholate, 0.1% SDS, 150 mM NaCl, 5 mM EDTA, and a protease inhibitor cocktail (45 mg/ml;
946 Roche, Cat. No. 11 873 580 001)] at 4 °C. Alternatively, adherent cells were harvested in RIPA buffer,
947 and kept on ice for 10 min. TA muscles and cell lysates were centrifuged at 12,000 g for 10 minutes at
948 4 °C, and the supernatants were collected for further analysis. For western blot analyses,
949 homogenates were separated in 8% polyacrylamide gels, transferred to Hybond nitrocellulose
950 membranes (Amersham Biosciences), and probed with specific antibodies targeting AR (Abcam,
951 ab108341, 1:500), α-TUBULIN (IGBMC, 1Tub2A2, 1:5000), and GAPDH (Cell Signaling, #2118, 1:5000).
952 Secondary antibodies conjugated to horseradish peroxidase (anit-Mouse-HPR, Cell Signalling, 7076S,
953 1:10,000; anit-Rabbit-HPR, Cell Signalling, 7074S, 1:10,000;) were detected using chemiluminescence
954 detection systems (GE Healthcare, Amersham, ImageQuant 800 or Imager 600). Protein quantification
955 was assessed by the FIJI/ImageJ distribution software (https://imagej.net/ImageJ) [90].

956

957 **Statistical analyses**

958 Data processing and analysis were conducted using DESeq2, Microsoft Excel and GraphPad Prism 9. In
959 all graphical representations, error bars indicate the standard error mean (SEM). Comparisons
960 between groups were performed using appropriate statistical tests, selected based on the number of
961 groups, data distribution (normality), variance homogeneity, and multiple comparisons. The specific
962 statistical tests applied are indicated in the figure legends. Statistical significance was defined as
963 follows: ns, $p > 0.05$ (non-significant); *, $p < 0.05$; **, $p < 0.01$; and ***, $p < 0.001$.

964

965 **Data availability**

966 Custom macro for CSA measurements and Sirius Red quantification are available on GitLab and
967 GitHub, respectively (CSA: the BIOP cellpose extension guide; Sirius Red: https://github.com/Hugues-
968 Jacobs/Fibrosis_analysis). All sequencing datasets generated in this study have been deposited in the
969 Gene Expression Omnibus (GEO) under the following accession numbers: GSE303611 for single-cell
970 RNA-seq (token: afmhqcmenpapfyl), GSE303612 for SMART-seq (token: slileymohzanlal), GSE303614
971 for bulk RNA-seq (token: chqloqugddwjvur), GSE303615 for CUT&RUN analysis at 5 dpi (token:
972 gtovmecctvyprot), GSE303618 for CUT&RUN analysis at 7 dpi (token: ynahwacgxtotdct), and
973 GSE303620 for CUT&RUN analysis in non-injured animals (token: mjufuemerzyhlwn).

974 **REFERENCES**

975 1. Charge, S.B. & Rudnicki, M.A. Cellular and molecular regulation of muscle regeneration.
976 *Physiol Rev* **84**, 209-238 (2004).
977 2. Goel, A.J., Rieder, M.K., Arnold, H.H., Radice, G.L. & Krauss, R.S. Niche Cadherins Control the
978 Quiescence-to-Activation Transition in Muscle Stem Cells. *Cell Rep* **21**, 2236-2250 (2017).
979 3. Rozo, M., Li, L. & Fan, C.M. Targeting beta1-integrin signaling enhances regeneration in aged
980 and dystrophic muscle in mice. *Nat Med* **22**, 889-896 (2016).
981 4. Seale, P. *et al.* Pax7 is required for the specification of myogenic satellite cells. *Cell* **102**, 777-
982 786 (2000).
983 5. Wang, Y.X. & Rudnicki, M.A. Satellite cells, the engines of muscle repair. *Nat Rev Mol Cell Biol*
984 **13**, 127-133 (2011).
985 6. Anderson, J.E. Key concepts in muscle regeneration: muscle "cellular ecology" integrates a
986 gestalt of cellular cross-talk, motility, and activity to remodel structure and restore function.
987 *Eur J Appl Physiol* **122**, 273-300 (2022).
988 7. Zhang, W., Liu, Y. & Zhang, H. Extracellular matrix: an important regulator of cell functions and
989 skeletal muscle development. *Cell Biosci* **11**, 65 (2021).
990 8. Koike, H., Manabe, I. & Oishi, Y. Mechanisms of cooperative cell-cell interactions in skeletal
991 muscle regeneration. *Inflamm Regen* **42**, 48 (2022).
992 9. Abou-Khalil, R. *et al.* Autocrine and paracrine angiopoietin 1/Tie-2 signaling promotes muscle
993 satellite cell self-renewal. *Cell Stem Cell* **5**, 298-309 (2009).
994 10. Kedlian, V.R. *et al.* Human skeletal muscle aging atlas. *Nat Aging* **4**, 727-744 (2024).
995 11. Su, J. *et al.* A novel atlas of gene expression in human skeletal muscle reveals molecular
996 changes associated with aging. *Skelet Muscle* **5**, 35 (2015).
997 12. Moiseeva, V. *et al.* Senescence atlas reveals an aged-like inflamed niche that blunts muscle
998 regeneration. *Nature* **613**, 169-178 (2023).
999 13. Day, K., Shefer, G., Shearer, A. & Yablonka-Reuveni, Z. The depletion of skeletal muscle
1000 satellite cells with age is concomitant with reduced capacity of single progenitors to produce
1001 reserve progeny. *Dev Biol* **340**, 330-343 (2010).
1002 14. Petermann-Rocha, F. *et al.* Global prevalence of sarcopenia and severe sarcopenia: a
1003 systematic review and meta-analysis. *J Cachexia Sarcopenia Muscle* **13**, 86-99 (2022).
1004 15. Munoz-Canoves, P., Neves, J. & Sousa-Victor, P. Understanding muscle regenerative decline
1005 with aging: new approaches to bring back youthfulness to aged stem cells. *FEBS J* **287**, 406-
1006 416 (2020).
1007 16. Rizk, J., Sahu, R. & Duteil, D. An overview on androgen-mediated actions in skeletal muscle
1008 and adipose tissue. *Steroids* **199**, 109306 (2023).
1009 17. Conboy, I.M. & Rando, T.A. The regulation of Notch signaling controls satellite cell activation
1010 and cell fate determination in postnatal myogenesis. *Dev Cell* **3**, 397-409 (2002).
1011 18. Seo, J.Y., Kim, J.H. & Kong, Y.Y. Unraveling the Paradoxical Action of Androgens on Muscle
1012 Stem Cells. *Mol Cells* **42**, 97-103 (2019).
1013 19. Niel, L., Willemsen, K.R., Volante, S.N. & Monks, D.A. Sexual dimorphism and androgen
1014 regulation of satellite cell population in differentiating rat levator ani muscle. *Dev Neurobiol*
1015 **68**, 115-122 (2008).
1016 20. Diel, P., Baadners, D., Schlupmann, K., Velders, M. & Schwarz, J.P. C2C12 myoblastoma cell
1017 differentiation and proliferation is stimulated by androgens and associated with a modulation
1018 of myostatin and Pax7 expression. *J Mol Endocrinol* **40**, 231-241 (2008).
1019 21. Chen, Y., Zajac, J.D. & MacLean, H.E. Androgen regulation of satellite cell function. *J Endocrinol*
1020 **186**, 21-31 (2005).
1021 22. Klose, A. *et al.* Castration induces satellite cell activation that contributes to skeletal muscle
1022 maintenance. *JCSM Rapid Commun* **1** (2018).
1023 23. Sakai, H. & Imai, Y. Cell-specific functions of androgen receptor in skeletal muscles. *Endocr J*
1024 **71**, 437-445 (2024).

1025 24. Sinha-Hikim, I., Taylor, W.E., Gonzalez-Cadavid, N.F., Zheng, W. & Bhasin, S. Androgen
1026 receptor in human skeletal muscle and cultured muscle satellite cells: up-regulation by
1027 androgen treatment. *J Clin Endocrinol Metab* **89**, 5245-5255 (2004).
1028 25. Ghaibour, K. *et al.* Androgen receptor coordinates muscle metabolic and contractile functions.
1029 *J Cachexia Sarcopenia Muscle* **14**, 1707-1720 (2023).
1030 26. Chambon, C. *et al.* Myocytic androgen receptor controls the strength but not the mass of limb
1031 muscles. *Proc Natl Acad Sci U S A* **107**, 14327-14332 (2010).
1032 27. Mourikis, P. & Tajbakhsh, S. Distinct contextual roles for Notch signalling in skeletal muscle
1033 stem cells. *BMC Dev Biol* **14**, 2 (2014).
1034 28. Pizza, F.X. & Buckley, K.H. Regenerating Myofibers after an Acute Muscle Injury: What Do We
1035 Really Know about Them? *Int J Mol Sci* **24** (2023).
1036 29. Oprescu, S.N., Yue, F., Qiu, J., Brito, L.F. & Kuang, S. Temporal Dynamics and Heterogeneity of
1037 Cell Populations during Skeletal Muscle Regeneration. *iScience* **23**, 100993 (2020).
1038 30. McKellar, D.W. *et al.* Large-scale integration of single-cell transcriptomic data captures
1039 transitional progenitor states in mouse skeletal muscle regeneration. *Commun Biol* **4**, 1280
1040 (2021).
1041 31. Yue, F. *et al.* Lipid droplet dynamics regulate adult muscle stem cell fate. *Cell Rep* **38**, 110267
1042 (2022).
1043 32. Morroni, J. *et al.* Injury-experienced satellite cells retain long-term enhanced regenerative
1044 capacity. *Stem Cell Res Ther* **14**, 246 (2023).
1045 33. Brun, C.E. *et al.* GLI3 regulates muscle stem cell entry into G(Alert) and self-renewal. *Nat*
1046 *Commun* **13**, 3961 (2022).
1047 34. Barsky, S.T. & Monks, D.A. The role of androgens and global and tissue-specific androgen
1048 receptor expression on body composition, exercise adaptation, and performance. *Biol Sex*
1049 *Differ* **16**, 28 (2025).
1050 35. Chinvattanachot, G., Rivas, D. & Duque, G. Mechanisms of muscle cells alterations and
1051 regeneration decline during aging. *Ageing Res Rev* **102**, 102589 (2024).
1052 36. Serra, C. *et al.* Testosterone improves the regeneration of old and young mouse skeletal
1053 muscle. *J Gerontol A Biol Sci Med Sci* **68**, 17-26 (2013).
1054 37. Oura, M. *et al.* Testosterone/androgen receptor antagonizes immobility-induced muscle
1055 atrophy through Inhibition of myostatin transcription and inflammation in mice. *Sci Rep* **15**,
1056 10568 (2025).
1057 38. Lai, Y. *et al.* Multimodal cell atlas of the ageing human skeletal muscle. *Nature* **629**, 154-164
1058 (2024).
1059 39. Tan, M.H., Li, J., Xu, H.E., Melcher, K. & Yong, E.L. Androgen receptor: structure, role in
1060 prostate cancer and drug discovery. *Acta Pharmacol Sin* **36**, 3-23 (2015).
1061 40. Gruntmanis, U. The Role of 5α-Reductase Inhibition in Men Receiving Testosterone
1062 Replacement Therapy. *JAMA* **307**, 968-970 (2012).
1063 41. Bartsch, G., Rittmaster, R.S. & Klocker, H. Dihydrotestosterone and the concept of 5alpha-
1064 reductase inhibition in human benign prostatic hyperplasia. *Eur Urol* **37**, 367-380 (2000).
1065 42. Dubois, V., Laurent, M., Boonen, S., Vanderschueren, D. & Claessens, F. Androgens and
1066 skeletal muscle: cellular and molecular action mechanisms underlying the anabolic actions.
1067 *Cell Mol Life Sci* **69**, 1651-1667 (2012).
1068 43. Sheppard, R.L., Spangenburg, E.E., Chin, E.R. & Roth, S.M. Androgen receptor polyglutamine
1069 repeat length affects receptor activity and C2C12 cell development. *Physiol Genomics* **43**,
1070 1135-1143 (2011).
1071 44. Fu, S., Lin, X., Yin, L. & Wang, X. Androgen receptor regulates the proliferation of myoblasts
1072 under appropriate or excessive stretch through IGF-1 receptor mediated p38 and ERK1/2
1073 pathways. *Nutr Metab (Lond)* **18**, 85 (2021).

1074 45. Fu, S., Hu, J., Wang, G., Qian, Z. & Wang, X. Androgen receptor regulates the differentiation of
1075 myoblasts under cyclic mechanical stretch and its upstream and downstream signals. *Int J Biol*
1076 *Macromol* **281**, 136257 (2024).
1077 46. Dubois, V. *et al.* Androgen Deficiency Exacerbates High-Fat Diet-Induced Metabolic Alterations
1078 in Male Mice. *Endocrinology* **157**, 648-665 (2016).
1079 47. Rocchi, A. *et al.* Glycolytic-to-oxidative fiber-type switch and mTOR signaling activation are
1080 early-onset features of SBMA muscle modified by high-fat diet. *Acta Neuropathol* **132**, 127-
1081 144 (2016).
1082 48. Campbell, M.D., Djukovic, D., Raftery, D. & Marcinek, D.J. Age-related changes of skeletal
1083 muscle metabolic response to contraction are also sex-dependent. *J Physiol* **603**, 69-86 (2025).
1084 49. Grevendonk, L. *et al.* Impact of aging and exercise on skeletal muscle mitochondrial capacity,
1085 energy metabolism, and physical function. *Nat Commun* **12**, 4773 (2021).
1086 50. Kobayashi, A., Azuma, K., Ikeda, K. & Inoue, S. Mechanisms Underlying the Regulation of
1087 Mitochondrial Respiratory Chain Complexes by Nuclear Steroid Receptors. *Int J Mol Sci* **21**
1088 (2020).
1089 51. Jomova, K. *et al.* Reactive oxygen species, toxicity, oxidative stress, and antioxidants: chronic
1090 diseases and aging. *Arch Toxicol* **97**, 2499-2574 (2023).
1091 52. Lee, J. *et al.* Androgen Deprivation Therapy-Induced Muscle Loss and Fat Gain Predict
1092 Cardiovascular Events in Prostate Cancer Patients. *J Cachexia Sarcopenia Muscle* **16**, e13844
1093 (2025).
1094 53. Argiles, J.M., Campos, N., Lopez-Pedrosa, J.M., Rueda, R. & Rodriguez-Manas, L. Skeletal
1095 Muscle Regulates Metabolism via Interorgan Crosstalk: Roles in Health and Disease. *J Am Med*
1096 *Dir Assoc* **17**, 789-796 (2016).
1097 54. Penvose, A., Keenan, J.L., Bray, D., Ramlall, V. & Siggers, T. Comprehensive study of nuclear
1098 receptor DNA binding provides a revised framework for understanding receptor specificity.
1099 *Nat Commun* **10**, 2514 (2019).
1100 55. Gelman, L. *et al.* Integrating nuclear receptor mobility in models of gene regulation. *Nucl*
1101 *Recept Signal* **4**, e010 (2006).
1102 56. Hager, G.L., Nagaich, A.K., Johnson, T.A., Walker, D.A. & John, S. Dynamics of nuclear receptor
1103 movement and transcription. *Biochim Biophys Acta* **1677**, 46-51 (2004).
1104 57. Stavreva, D.A. *et al.* Nuclear Receptors Dynamics and Gene Regulation in Response to
1105 Ultradian Hormone Pulses. *Endocrinology* **166**, bqaf043.034 (2025).
1106 58. Forouhan, M. *et al.* AR cooperates with SMAD4 to maintain skeletal muscle homeostasis. *Acta*
1107 *Neuropathol* **143**, 713-731 (2022).
1108 59. Nath, S.R. *et al.* Androgen receptor polyglutamine expansion drives age-dependent quality
1109 control defects and muscle dysfunction. *J Clin Invest* **128**, 3630-3641 (2018).
1110 60. Arnold, F.J., Pluciennik, A. & Merry, D.E. Impaired Nuclear Export of Polyglutamine-Expanded
1111 Androgen Receptor in Spinal and Bulbar Muscular Atrophy. *Sci Rep* **9**, 119 (2019).
1112 61. Shiina, H. *et al.* Premature ovarian failure in androgen receptor-deficient mice. *Proc Natl Acad*
1113 *Sci U S A* **103**, 224-229 (2006).
1114 62. Murphy, M.M., Lawson, J.A., Mathew, S.J., Hutcheson, D.A. & Kardon, G. Satellite cells,
1115 connective tissue fibroblasts and their interactions are crucial for muscle regeneration.
1116 *Development* **138**, 3625-3637 (2011).
1117 63. Tosic, M. *et al.* Lsd1 regulates skeletal muscle regeneration and directs the fate of satellite
1118 cells. *Nat Commun* **9**, 366 (2018).
1119 64. Chenu, C. *et al.* Testosterone Prevents Cutaneous Ischemia and Necrosis in Males Through
1120 Complementary Estrogenic and Androgenic Actions. *Arterioscler Thromb Vasc Biol* **37**, 909-
1121 919 (2017).
1122 65. Rovito, D. *et al.* Myod1 and GR coordinate myofiber-specific transcriptional enhancers. *Nucleic*
1123 *Acids Res* **49**, 4472-4492 (2021).

1124 66. Simon, A. *et al.* Transcriptomic characterization of postnatal muscle maturation. *Dis Model*
1125 *Mech* **18** (2025).
1126 67. Cigrang, M. *et al.* Pan-inhibition of super-enhancer-driven oncogenic transcription by next-
1127 generation synthetic ecteinascidins yields potent anti-cancer activity. *Nat Commun* **16**, 512
1128 (2025).
1129 68. Ghaibour, K. *et al.* An Efficient Protocol for CUT&RUN Analysis of FACS-Isolated Mouse
1130 Satellite Cells. *J Vis Exp* (2023).
1131 69. Janssens, D.H. *et al.* Automated in situ chromatin profiling efficiently resolves cell types and
1132 gene regulatory programs. *Epigenetics Chromatin* **11**, 74 (2018).
1133 70. Langmead, B. & Salzberg, S.L. Fast gapped-read alignment with Bowtie 2. *Nat Methods* **9**, 357-
1134 359 (2012).
1135 71. Ramirez, F., Dundar, F., Diehl, S., Gruning, B.A. & Manke, T. deepTools: a flexible platform for
1136 exploring deep-sequencing data. *Nucleic Acids Res* **42**, W187-191 (2014).
1137 72. Quinlan, A.R. & Hall, I.M. BEDTools: a flexible suite of utilities for comparing genomic features.
1138 *Bioinformatics* **26**, 841-842 (2010).
1139 73. Meers, M.P., Tenenbaum, D. & Henikoff, S. Peak calling by Sparse Enrichment Analysis for
1140 CUT&RUN chromatin profiling. *Epigenetics Chromatin* **12**, 42 (2019).
1141 74. Zhang, Y. *et al.* Model-based analysis of ChIP-Seq (MACS). *Genome Biol* **9**, R137 (2008).
1142 75. Ye, T. *et al.* seqMINER: an integrated ChIP-seq data interpretation platform. *Nucleic Acids Res*
1143 **39**, e35 (2011).
1144 76. Cai, Q. *et al.* LSD1 inhibition circumvents glucocorticoid-induced muscle wasting of male mice.
1145 *Nat Commun* **15**, 3563 (2024).
1146 77. Livak, K.J. & Schmittgen, T.D. Analysis of relative gene expression data using real-time
1147 quantitative PCR and the 2(-Delta Delta C(T)) Method. *Methods* **25**, 402-408 (2001).
1148 78. Dobin, A. *et al.* STAR: ultrafast universal RNA-seq aligner. *Bioinformatics* **29**, 15-21 (2013).
1149 79. Anders, S., Pyl, P.T. & Huber, W. HTSeq--a Python framework to work with high-throughput
1150 sequencing data. *Bioinformatics* **31**, 166-169 (2015).
1151 80. Love, M.I., Huber, W. & Anders, S. Moderated estimation of fold change and dispersion for
1152 RNA-seq data with DESeq2. *Genome Biol* **15**, 550 (2014).
1153 81. Szklarczyk, D. *et al.* The STRING database in 2023: protein-protein association networks and
1154 functional enrichment analyses for any sequenced genome of interest. *Nucleic Acids Res* **51**,
1155 D638-D646 (2023).
1156 82. Wang, J., Duncan, D., Shi, Z. & Zhang, B. WEB-based GEne SeT AnaLysis Toolkit (WebGestalt):
1157 update 2013. *Nucleic Acids Res* **41**, W77-83 (2013).
1158 83. de Hoon, M.J., Imoto, S., Nolan, J. & Miyano, S. Open source clustering software.
1159 *Bioinformatics* **20**, 1453-1454 (2004).
1160 84. Lu, Y., Lu, S., Fotouhi, F., Deng, Y. & Brown, S.J. Incremental genetic K-means algorithm and its
1161 application in gene expression data analysis. *BMC Bioinformatics* **5**, 172 (2004).
1162 85. Raine, A., Liljedahl, U. & Nordlund, J. Data quality of whole genome bisulfite sequencing on
1163 Illumina platforms. *PLoS One* **13**, e0195972 (2018).
1164 86. Lun, A.T.L. *et al.* EmptyDrops: distinguishing cells from empty droplets in droplet-based single-
1165 cell RNA sequencing data. *Genome Biol* **20**, 63 (2019).
1166 87. Satija, R., Farrell, J.A., Gennert, D., Schier, A.F. & Regev, A. Spatial reconstruction of single-cell
1167 gene expression data. *Nat Biotechnol* **33**, 495-502 (2015).
1168 88. Jin, S. *et al.* Inference and analysis of cell-cell communication using CellChat. *Nat Commun* **12**,
1169 1088 (2021).
1170 89. Riba, A. *et al.* Cell cycle gene regulation dynamics revealed by RNA velocity and deep-learning.
1171 *Nat Commun* **13**, 2865 (2022).
1172 90. Schneider, C.A., Rasband, W.S. & Eliceiri, K.W. NIH Image to ImageJ: 25 years of image analysis.
1173 *Nat Methods* **9**, 671-675 (2012).

1174

1175 **ACKNOWLEDGMENTS**

1176 We thank Dr. J. Laporte (IGBMC) for generously providing the LHCN-M2 and C79 cell lines. We are
1177 grateful to Anastasia Bannwarth, Nikola Djordjevic, and Régis Lutzing for their valuable technical
1178 support, and Valentine Gilbart, Tao Ye and Céline Keime for excellent bioinformatics assistance. We
1179 extend our gratitude to Mohammed Selloum and Aurélie Aubertin for their valuable scientific
1180 expertise on biochemical analyses. We are grateful to Prof. S. Kato for providing the AR floxed mice,
1181 and Prof. G. Kardon for the *Pax7*-CreER^{T2} line. We acknowledge the support of the IGBMC core
1182 facilities, including the animal facility, microscopy and electron microscopy platforms, biochemistry,
1183 cell culture service, flow cytometry, and histopathology services, as well as the Mouse Clinical Institute
1184 (ICS, Illkirch-Graffenstaden, France) and GenomEast facility, a member of the 'France Génomique'
1185 consortium (ANR-10-INBS-0009).

1186 This work was supported by the Interdisciplinary Thematic Institute IMCBio as part of the ITI 2021-
1187 2028 program of the University of Strasbourg, the Centre National pour la Recherche Scientifique
1188 (CNRS), Institut national de la santé et de la recherche médicale (Inserm), from IdEx Unistra (ANR-10-
1189 IDEX-0002), SFRI-STRAT'US (ANR 20-SFRI-0012) and EUR IMCBio (ANR-17-EURE-0023) projects, under
1190 the framework of the French Investments for the Future Programme. Additional support was provided
1191 by Inserm, CNRS, Unistra, IGBMC, AFM-Téléthon (grant application #24376), and the Agence Nationale
1192 de la Recherche (ANR-10-BLAN-1108, ANR-24-CE14-0247-01). J.G.R. received funding from the
1193 Programme CDFA-07-22 from the Université franco-allemande and Ministère de l'Enseignement
1194 Supérieur de la Recherche et de l'Innovation. K.C.G. received funding by the Association pour la
1195 Recherche à l'IGBMC (ARI), E.C by MESRI, Q.C by ANR (ANDROMETAMUS, ANR-24-CE14-0247-01), and
1196 R.S. by IMCBio. Anastasia Bannwarth received funding from AFM-Téléthon (grant application #24376)
1197 for technical assistance.

1198

1199 **AUTHOR CONTRIBUTIONS**

1200 D.D., J.G.R., and K.C.G. formulated the initial hypothesis. J.G.R., K.C.G., S.S.C., A.B., Q.C., G. R., E.C., and
1201 R.S. carried out functional, molecular, and histological experiments. D.D., J.G.R., N.M., and G.Z.
1202 executed bioinformatics analyses. J.G.R., N.M., H.J., and E.G. took responsibility of imaging analyses.
1203 A.F. conducted *in situ* myofiber contraction experiments. J-F.A. and C.F. provided DHT pellets and
1204 performed initial *in vivo* tests. J.G.R., K.C.G., D.M., and D.D. took primary responsibility for data
1205 analysis and writing the manuscript.

1206

1207 **Declaration of interests**

1208 The authors declare no competing interests.

ETHICS DECLARATIONS

Competing interests

The authors declare no competing interests.

1212 **FIGURE LEGENDS**

1213 **Figure 1: Absence of MuSC-AR impairs muscle regenerative capacities at young age.**

1214 **(A)** Representative hematoxylin and eosin (H&E) staining of tibialis anterior (TA) muscles of young
1215 control and $AR^{(i)sat-/Y}$ male mice under non-injured (NI) condition, and at 7 days post-injury (7 dpi).
1216 Black arrows indicate centrally nucleated fibers. Cyan arrows point to immune infiltration. Yellow
1217 arrows denote necrotic fibers. Green arrows show interstitial space. Pink arrows label misshaped
1218 regenerating myofibers. Orange arrows mark fibrosis. Scale bars, 75 µm.

1219 **(B)** Ultrastructure analysis of NI and 7-days-injured TA of young control and $AR^{(i)sat-/Y}$ male mice. Z: Z-
1220 line, M: M-line, I: I-bands, A: A-band. Black arrows indicate M-line disturbances. Red arrows point to
1221 Z-line disruption. Pink arrows depict T-tubules misalignments. Orange arrows denote fibrosis. Green
1222 arrows show the A-band placement. Yellow arrows label the I-bands placements. Scale bars, 1 µm.

1223 **(C)** Distribution of myofibers cross-section area (CSA) in TA muscles of young control and $AR^{(i)sat-/Y}$ male
1224 mice 7 dpi. Data are presented as mean ± SEM. Statistical test used Two-way ANOVA with Sidak's
1225 correction; * = $p < 0.05$; ** = $p < 0.01$.

1226 **(D)** *In situ* single-fiber isometric force of 28-days-injured TA of young control and $AR^{(i)sat-/Y}$ male mice.
1227 Data are presented as mean ± SEM. Statistical test used was two-tailed Mann-Whitney test; * = $p <$
1228 0.05.

1229 **(E-F)** Representative immunofluorescent labeling of PAX7 (in red) **(E)**, and corresponding
1230 quantification of the number of PAX7-positive cells **(F)**, in 7-days-injured TA of young control and
1231 $AR^{(i)sat-/Y}$ male mice. White arrows point to PAX7-positive cells. Nuclei were stained with DAPI. Data are
1232 presented as mean ± SEM. Statistical test used is two-tailed Mann-Whitney test; ** = $p < 0.01$.

1233 **(G-H)** Heatmap depicting the mean centered normalized expression of indicated genes selected from
1234 bulk RNA-sequencing analysis performed in 7-days-injured TA of young control and $AR^{(i)sat-/Y}$ male mice
1235 **(G)**, and corresponding pathway analysis **(H)**.

1236 **(I)** Violin plots representing the normalized read counts of the indicated genes, selected from bulk
1237 RNA-sequencing analysis performed in 7-days-injured TA of young control and $AR^{(i)sat-/Y}$ male mice.
1238 Statistical test used is Wald test; ** = $p < 0.01$; *** = $p < 0.001$.

1239 **(J)** Representative immunofluorescent detection of DMD (in red), in 7-days-injured TA of young
1240 control and $AR^{(i)sat-/Y}$ male mice. Nuclei were stained with DAPI. White arrows depict fibers emerging
1241 within other fibers. Scale bars, 100 µm.

1242 **(K)** Representative immunofluorescent detection of DMD (in red), and sarcomeric alpha actinin
1243 (ACTN1) (in green), in 7-days-injured transversal and longitudinal sections of TA of young control and
1244 $AR^{(i)sat-/Y}$ male mice. Nuclei were stained with DAPI. White arrows point to nuclei. Yellow arrows denote

1245 sarcolemma discontinuation. Red arrows show ACTN1 aggregates. Pink arrows denote stairs-shape in
1246 regenerating fibers. Scale bars, 50 µm.
1247 **(L-M)** Representative immunofluorescent detection of embryonic myosin (MYH3) (in green), and
1248 LAMA2 (in magenta) **(L)**, and corresponding quantification of the number of MYH3-positive cells **(M)**
1249 in 5- and 7-days-injured TA of young control and $AR^{(i)sat-/Y}$ male mice. Nuclei were stained with DAPI.
1250 Scale bars, 85 µm. Data are presented as mean ± SEM. Statistical test used is Two-way ANOVA with
1251 Tukey correction; ns, non-significant; ** = $p < 0.01$; *** = $p < 0.001$.
1252 **(N-O)** Violin plots representing the normalized read counts of the indicated genes encoding myosin
1253 heavy chain (*Myhs*) isoforms **(N)**, or subunits of the electron transport chain complexes **(O)** selected
1254 from bulk RNA-sequencing analysis performed in 7-days-injured TA of young control and $AR^{(i)sat-/Y}$ male
1255 mice. Statistical test used is Wald test; * = $p < 0.05$; ** = $p < 0.01$; *** = $p < 0.001$.
1256 **(P)** Representative histochemical staining of NADH dehydrogenase (NADH-DH) and COX activities in
1257 7-days-injured TA of young control and $AR^{(i)sat-/Y}$ male mice. Oxidative and intermediate fibers are
1258 darkly and moderately stained, respectively; glycolytic fibers are lightly stained. Scale bars, 200 µm.
1259 **(Q)** Mitochondrial respiration profile of vehicle and 100 nM flutamide-treated LHCN-M2 cells,
1260 assessed using the Seahorse Mito Stress Test, following sequential injection of oligomycin, carbonyl
1261 cyanide-p-trifluoromethoxyphenylhydrazone (FCCP), and rotenone/AA, and expressed as oxygen
1262 consumption rate (OCR). Data are normalized to total nuclear counts, and presented as mean ± SEM.
1263 Statistical test used was two-tailed Mann-Whitney test; * = $p < 0.05$.
1264
1265 **Figure 2: Characterization of AR cistrome and transcriptome in MuSC at young age.**
1266 **(A)** Heatmap depicting the mean centered normalized expression of indicated genes selected from
1267 bulk RNA-sequencing analysis performed in 7-days-injured TA of young control and $AR^{(i)sat-/Y}$ male mice.
1268 **(B)** Pathway analysis of down- and up-regulated genes in 7-days-injured TA of young control and
1269 $AR^{(i)sat-/Y}$ male mice.
1270 **(C-D)** Violin plots representing the normalized read counts of the indicated genes, selected from bulk
1271 RNA-sequencing analysis performed in 7-days-injured TA of young control and $AR^{(i)sat-/Y}$ male mice.
1272 Statistical test used is Wald test; * = $p < 0.05$; ** = $p < 0.01$; *** = $p < 0.001$.
1273 **(E)** HOMER known and *de novo* motif analyses of AR-bound DNA sequences from 7-day-injured TA of
1274 young male mice.
1275 **(F)** Pathway analysis performed on AR target genes identified by CUT&RUN in MuSC of 7-day-injured
1276 TA of young male mice. Pathways of interest are squared in red.
1277 **(G)** Cumulative number of down-regulated genes, and up-regulated genes in MuSC of 7-day-injured
1278 TA of young male mice, with an AR peak located at the indicated distances from their TSS.

1279 **(H)** AR localization at the *Ar*, *Fzd4*, *Kdmc4*, *Myh1*, *Tead1*, and *Mylk4* loci, with binding sites shown in
1280 red.
1281
1282 **Figure 3: MuSC microenvironment is altered in the absence of AR.**
1283 **(A-B)** Uniform manifold approximation and projection (UMAP) visualization of single cells **(A)**, and
1284 respective percentage of cell types **(B)**, from 5-days-injured control and $AR^{(i)sat-/Y}$ TA of young mice,
1285 colored by cluster identity.
1286 **(C-D)** Percentage of macrophages **(C)**, immune cells, FAPs and MuSC **(D)**, in 5-days-injured TA of young
1287 control and $AR^{(i)sat-/Y}$ mice, analyzed from flow-cytometry data conducted at the indicated time-point.
1288 Data are presented as mean ± SEM. Statistical test used was two-tailed Mann-Whitney test; ns, non-
1289 significant; * = $p < 0.05$, *** = $p < 0.001$.
1290 **(E)** Violin plot of *Ar* transcript levels in the indicated cell populations identified from 5-days-injured TA
1291 of young control and $AR^{(i)sat-/Y}$ mice.
1292 **(F)** Schematic diagram of cell-cell communication between MuSC and other TA constitutive cells types
1293 in 5-days-injured TA of young control and $AR^{(i)sat-/Y}$ mice. Arrow thickness indicates the relative
1294 interaction strength between populations, as inferred from ligand-receptor expression analysis.
1295 **(G-H)** Violin plots representing the transcript levels of macrophage type-1 **(G)**, and macrophage type-
1296 2 markers **(H)**, selected from scRNA-seq analysis performed in 5-days-injured TA of young control and
1297 $AR^{(i)sat-/Y}$ mice.
1298 **(I)** Percentage of immune cells, FAPs and MuSC, in 7-days-injured TA of young control and $AR^{(i)sat-/Y}$
1299 mice, analyzed from flow-cytometry data conducted at the indicated time-point. Data are presented
1300 as mean ± SEM. Statistical test used was two-tailed Mann-Whitney test; ns, non-significant; ** = $p <$
1301 0.01; *** = $p < 0.001$.
1302 **(J-K)** Representative immunofluorescent detection of F4/80 (in green) **(J)**, and corresponding
1303 quantification of mean fluorescence intensity (MFI) of F4/80 signal **(K)**, in 7-days-injured TA of young
1304 control and $AR^{(i)sat-/Y}$ mice. White arrows depict inter-fiber macrophages. Red arrows point to intra-
1305 fibers macrophages. Nuclei were stained with DAPI. Scale bars, 100 µm for the main, 30 µm for
1306 magnified inset. Statistical test used was two-tailed Mann-Whitney test; ns, non-significant.
1307 **(L)** Representative Sirius Red histochemical staining visualized under brightfield (upper panel), and
1308 polarized light (lower panel), in 7-days-injured TA of young control and $AR^{(i)sat-/Y}$ mice. Black arrows
1309 point to collagen fibers deposition. White arrows depict type I collagen fibers. Cyan blue arrows
1310 indicate type III collagen fibers. Scale bars, 250 µm for the main, 90 µm for magnified inset.

1311 **(M-N)** Quantification of Sirius Red area from brightfield analysis **(M)**, and fibrosis composition **(N)** of
1312 7-days-injured TA of young control and $AR^{(i)sat-/Y}$ mice. Data are presented as mean ± SEM. Statistical
1313 test used was two-tailed Mann-Whitney test; ns, non-significant; ** = $p < 0.01$.
1314 **(O-P)** Representative immunofluorescent detection of perilipin (PLIN1) (red) **(O)**, and corresponding
1315 quantification **(P)**, in 5- and 7-days-injured TA of young control and $AR^{(i)sat-/Y}$ mice. White arrows point
1316 to adipocytes. Nuclei were stained with DAPI. Scale bars, 100 µm. Data are presented as mean ± SEM.
1317 Statistical test used Two-way ANOVA with Sidak's correction; * = $p < 0.05$.
1318 **(Q)** Schematic overview of the influence of AR signaling in MuSC within the regenerative niche at
1319 young age. MuSC-AR contributes to the orchestration of the immune response during muscle
1320 regeneration by ensuring the timely coordination of pro- and anti-inflammatory phases. In parallel,
1321 MuSC-AR signaling restrains FAPs from excessive extracellular matrix deposition and adipogenic
1322 differentiation. Green arrows indicate activation, red arrows indicate inhibition, and black arrows
1323 represent undefined interactions.
1324
1325 **Figure 4: AR deficiency in MuSC favors symmetric differentiation over asymmetric division or**
1326 **symmetric self-renewal**
1327 **(A)** UMAP visualization of MuSC reclusters from 5-days-injured control and $AR^{(i)sat-/Y}$ TA of young mice,
1328 colored by cluster identity.
1329 **(B)** Violin plots representing the expression level of indicated genes in MuSC reclusters, selected from
1330 scRNA-seq analysis performed in 5-days-injured TA of young control and $AR^{(i)sat-/Y}$ mice.
1331 **(C)** Cell cycle distribution across MuSC reclusters in 5-days-injured TA of young control and $AR^{(i)sat-/Y}$
1332 mice, showing the proportion of cells in G1, S, and G2/M phases.
1333 **(D-F)** Representative immunofluorescent detection of PAX7 (magenta), and KI67 (green) **(D)**, and
1334 corresponding quantifications in 5- **(E)** and 7-days **(F)** injured TA of young control and $AR^{(i)sat-/Y}$ mice.
1335 Nuclei were stained with DAPI. Scale bars, 100 µm for the main, 30 µm for magnified inset. Statistical
1336 test used is Two-way ANOVA with Tukey correction; ns, non-significant; * = $p < 0.05$; *** = $p < 0.001$.
1337 **(G-I)** Representative immunofluorescent detection of PAX7 (magenta) and MYOG (green), and
1338 corresponding quantifications in 5- **(H)** and 7-days **(I)** injured TA of young control and $AR^{(i)sat-/Y}$ mice.
1339 Nuclei were stained with DAPI. Scale bars, 100 µm for the main, 30 µm for magnified inset. Data are
1340 presented as mean ± SEM. Statistical test used is Two-way ANOVA with Tukey correction; ns, non-
1341 significant; * = $p < 0.05$; *** = $p < 0.001$.
1342 **(J-K)** Representative immunofluorescent detection of MYOG (in magenta) and KI67 (in green) **(J)**, and
1343 corresponding quantification of the number of MYOG/KI67-double positive cells per field of injury **(K)**,
1344 in 5- and 7-days-injured TA of young control and $AR^{(i)sat-/Y}$ mice. White arrows depict MYOG/KI67-

1345 double positive cells. Nuclei were stained with DAPI. Scale bars, 75 µm for the main, 30 µm for
1346 magnified inset. Data are presented as mean ± SEM. Statistical test used is Two-way ANOVA with
1347 Tukey correction; ** = $p < 0.01$; *** = $p < 0.001$.
1348 **(L)** Representative HE staining of TA muscles of young control and $AR^{(i)sat-/Y}$ mice, 7 (single injury) and
1349 28+7 (double injury) days after injury. Cyan blue arrows denote inflammatory cells. Green arrows point
1350 to interstitial space. Black arrows depict central nuclei. Pink arrows show misshaped fibers. Scale bars,
1351 100 µm.
1352 **(M)** Representative immunofluorescent detection of DMD (red), and PAX7 (green), of 28+7-days-
1353 injured young control and $AR^{(i)sat-/Y}$ mouse TA. Scale bars, 50 µm.
1354 **(N)** Quantification of the number of PAX7-positive cells in 28+7-days-injured young control and $AR^{(i)sat-}$
1355 $^{/Y}$ mouse TA. Data are presented as mean ± SEM. Statistical test used was two-tailed Mann-Whitney
1356 test; * = $p < 0.05$.
1357 **(O)** Schematic overview of MuSC-autonomous regulation by AR signaling at young age. AR activity in
1358 MuSC promotes self-renewing divisions (maintenance plane), leading to the preservation of the stem
1359 cell pool. Conversely, AR signaling inhibits commitment divisions (commitment plane). Green arrow
1360 indicate activation, and red arrows indicate inhibition.
1361
1362 **Figure 5: MuSC-AR exhibits time-dependent binding to target genes following injury**
1363 **(A)** HOMER known and *de novo* motif analyses of AR-bound DNA sequences from 5-day-injured TA of
1364 young male mice.
1365 **(B)** Pathway analysis performed on AR common target genes identified in MuSC of 5-day-injured TA
1366 of young male mice.
1367 **(C-D)** Cumulative number of down-regulated genes **(C)**, and up-regulated genes **(D)** in MuSC of 5-day-
1368 injured TA of young male mice, with an AR peak located at the indicated distances from their TSS.
1369 **(E)** AR localization at the *Clock*, *Eif2d*, and *Psma4* loci. Binding sites are indicated in red.
1370 **(F)** Average tag density profiles, and corresponding tag density map of AR in NI, 5- and 7-days injured
1371 TA muscles of young male mice, +/− 2 kb from the AR peak center.
1372 **(G)** Overlap among genes bound by AR, in NI, 5- and 7-days injured TA muscles of young male mice.
1373 **(H)** AR localization in MuSC in NI, 5- and 7-days injured TA muscles of young male mice, at indicated
1374 loci.
1375 **(I)** Schematic overview of AR-mediated temporal regulation and chromatin binding dynamics in MuSC
1376 during regeneration at young age. AR displays stage-specific chromatin occupancy throughout muscle
1377 regeneration. In uninjured muscle, MuSC-AR supports homeostasis. Following injury, AR translocates

1378 to genomic regions that drive regenerative programs, favoring genes involved in MuSC activation and
1379 proliferation at 5 dpi, and shifting toward loci promoting differentiation and maturation by 7 dpi.
1380
1381 **Figure 6: Age-related androgen decline alters skeletal muscle repair machinery**
1382 **(A)** Serum testosterone levels of control male mice at indicated time-points (young, mid-old and old).
1383 Basal level is represented by a dashed line. Data are presented as mean ± SEM. Statistical test used is
1384 Ordinary One-way ANOVA relative to 2-month-old mice. ns, non-significant; * = $p < 0.05$; ** = $p < 0.01$.
1385 **(B)** Relative *Ar* transcript levels in TA muscles of control mice at indicated time-points (young, mid-old
1386 and old). Data are presented as mean ± SEM. Statistical test used is Ordinary One-way ANOVA. *** =
1387 $p < 0.001$.
1388 **(C-D)** Representative western blot analysis **(C)**, and corresponding quantification of the indicated
1389 proteins **(D)** in TA of young and old control male mice. GAPDH was used as a loading control. Data are
1390 presented as mean ± SEM. Statistical test used was two-tailed Mann-Whitney test; *** = $p < 0.001$.
1391 **(E)** Relative *Pax7* transcript levels in TA muscles from young and old control male mice. Data are
1392 presented as mean ± SEM. Statistical test used was two-tailed Mann-Whitney test; * = $p < 0.05$.
1393 **(F)** Representative hematoxylin and eosin (H&E) staining of TA muscles of control and $AR^{(i)sat-/Y}$ old
1394 male mice under non-injured (NI) condition, and at 7 dpi. Black arrows indicate centrally nucleated
1395 fibers. Blue arrows point to immune infiltration. Yellow arrows denote necrotic fibers. Green arrows
1396 show interstitial space. Pink arrows label misshaped regenerating myofibers. Orange arrows mark
1397 fibrosis. Scale bars, 75 µm.
1398 **(G)** Ultrastructure analysis of NI and 7-days-injured TA of control and $AR^{(i)sat-/Y}$ old male mice. Black
1399 arrows indicate M-line disturbances. Red arrows point to Z-line disruption. Pink arrows depict T-
1400 tubules misalignments. Orange arrows denote fibrosis. Green arrows show the A-band placement.
1401 Yellow arrows label the I-bands placements. Scale bars, 1 µm.
1402 **(H)** Representative immunofluorescent labeling of PAX7 (in red), and corresponding quantification of
1403 the number of PAX7-positive cells in 7-days-injured TA of control and $AR^{(i)sat-/Y}$ old male mice. White
1404 arrows point to PAX7-positive cells. Nuclei were stained with DAPI. Data are presented as mean ± SEM.
1405 Statistical test used is two-tailed Mann-Whitney test; * = $p < 0.05$.
1406 **(I)** Representative immunofluorescent detection of DMD (in red), in 7-days-injured TA of control and
1407 $AR^{(i)sat-/Y}$ old male mice. Nuclei were stained with DAPI. Scale bars, 100 µm.
1408 **(J)** Representative histochemical staining of NADH dehydrogenase (NADH-DH) and COX activities in 7-
1409 days-injured TA of control and $AR^{(i)sat-/Y}$ old male mice. Oxidative and intermediate fibers are darkly
1410 and moderately stained, respectively; glycolytic fibers are lightly stained. Scale bars, 200 µm.

1411 **(K)** Representative Sirius Red histochemical staining visualized under brightfield, and corresponding
1412 quantification of Sirius Red area, in 7-days-injured TA of control and $AR^{(i)sat-/Y}$ old male mice. Black
1413 arrows point to collagen fibers deposition. Scale bars, 250 µm. Data are presented as mean ± SEM.
1414 Statistical test used was two-tailed Mann-Whitney test; *** = p < 0.001.
1415 **(L)** Representative immunofluorescent detection of perilipin (PLIN1) (green), and corresponding
1416 quantification of total number of adipocytes, in 5- and 7-days-injured TA of control and $AR^{(i)sat-/Y}$ old
1417 mice. White arrows point to adipocytes. Nuclei were stained with DAPI. Scale bars, 100 µm. Data are
1418 presented as mean ± SEM. Statistical test used is Two-way ANOVA with Tukey correction; ns = non-
1419 significant; * = p< 0.05.
1420 **(M)** Representative HE staining, and corresponding quantification of the average number of central
1421 nuclei of TA muscles of control Sham-operated or DHT-supplemented old male mice, 7 dpi. Cyan blue
1422 arrows point to immune infiltration. Black arrows denote central nuclei. White arrows show central
1423 or parallel nuclei alignments. Scale bars, 150 µm for transverse, and 100 µm for longitudinal sections.
1424 Data are presented as mean ± SEM. Statistical test used was two-tailed Mann-Whitney test; * = p <
1425 0.05.
1426 **(N-Q)** Representative immunofluorescent detections of PAX7 (green) **(N)**, PAX7 (green) and KI67
1427 (magenta) **(O)**, MYOG (red) **(P)**, and F4/80 (green) **(Q)**, and corresponding quantifications per field of
1428 injury in TA muscles of control Sham-operated or DHT-supplemented old male mice, 7 dpi. Nuclei were
1429 stained with DAPI. Scale bars, 50 µm (N), 20 µm (O), 20 µm (P), and 50 µm (Q). Data are presented as
1430 mean ± SEM. Statistical test used was two-tailed Mann-Whitney test; ns, non-significant.
1431
1432 **Figure 7: Androgen receptor governs MuSC function in aged muscle through mechanisms that differ**
1433 **from those operating in the young.**
1434 **(A-B)** Heatmap depicting the mean centered normalized expression of down- and upregulated genes
1435 from SMART-seq analysis performed on control MuSC FACS-isolated from 7-day-injured TA of old and
1436 young mice **(A)**, and corresponding gene ontology enrichment **(B)**.
1437 **(C)** Violin plots representing the normalized read counts of the indicated genes, selected from SMART-
1438 seq analysis performed control MuSC FACS-isolated from 7-day-injured TA of old and young mice.
1439 Statistical test used is Wald test; * = p < 0.05; ** = p < 0.01; *** = p < 0.001.
1440 **(D)** Venn diagrams showing intersected genes among differentially expressed genes in MuSC of control
1441 old mice and $AR^{(i)sat-/Y}$ young mice.
1442 **(E-F)** Cumulative number of down-regulated genes **(E)**, and up-regulated genes **(F)** in MuSC of 7-day-
1443 injured TA of old male mice, with an AR peak located at the indicated distances from their TSS.

1444 **(G)** Venn diagrams showing intersected genes with AR peaks among differentially expressed genes in
1445 MuSC of control old mice and $AR^{(i)sat-/Y}$ young mice.
1446 **(H)** Relative *AR* transcript levels in control LHCN-M2 and C79 myoblasts. Data are presented as mean
1447 ± SEM. Statistical test used was two-tailed Mann-Whitney test; ** = $p < 0.01$.
1448 **(I-J)** Representative western blot analysis **(I)**, and corresponding quantification of the indicated
1449 proteins **(J)** in control LHCN-M2 and C79 myoblasts. α-TUBULIN (TUB) was used as a loading control.
1450 Data are presented as mean ± SEM. Statistical test used was two-tailed Mann-Whitney test; * = $p <$
1451 0.05.
1452 **(K)** Representative immunofluorescent detection of PAX7 (in green) and AR (in red), in LHCN-M2 and
1453 C79 cells. Scale bars, 100 µm for the main, 10 µm for magnified inset.
1454 **(L)** Quantification of the percentage of high- and low/non-proliferative control LHCN-M2 and C79
1455 myoblasts as determined by CellTrace analysis. Data are presented as mean ± SEM. Statistical test
1456 used is Two-way ANOVA with Tukey correction; *** = $p< 0.001$.
1457 **(M)** Representative brightfield images of control (CTR), AR-siRNA transfected (siRNA-hAR) and AR-
1458 plasmid transfected (OE-hAR) LHCN-M2 and C79 cells, 0, 3- and 5-days post-differentiation (dpd).
1459 Black arrows show fibroblast-like non-differentiated cells. Red arrows label spindle-like differentiated
1460 cells. Scale bars, 100 µm.

FIGURE 1

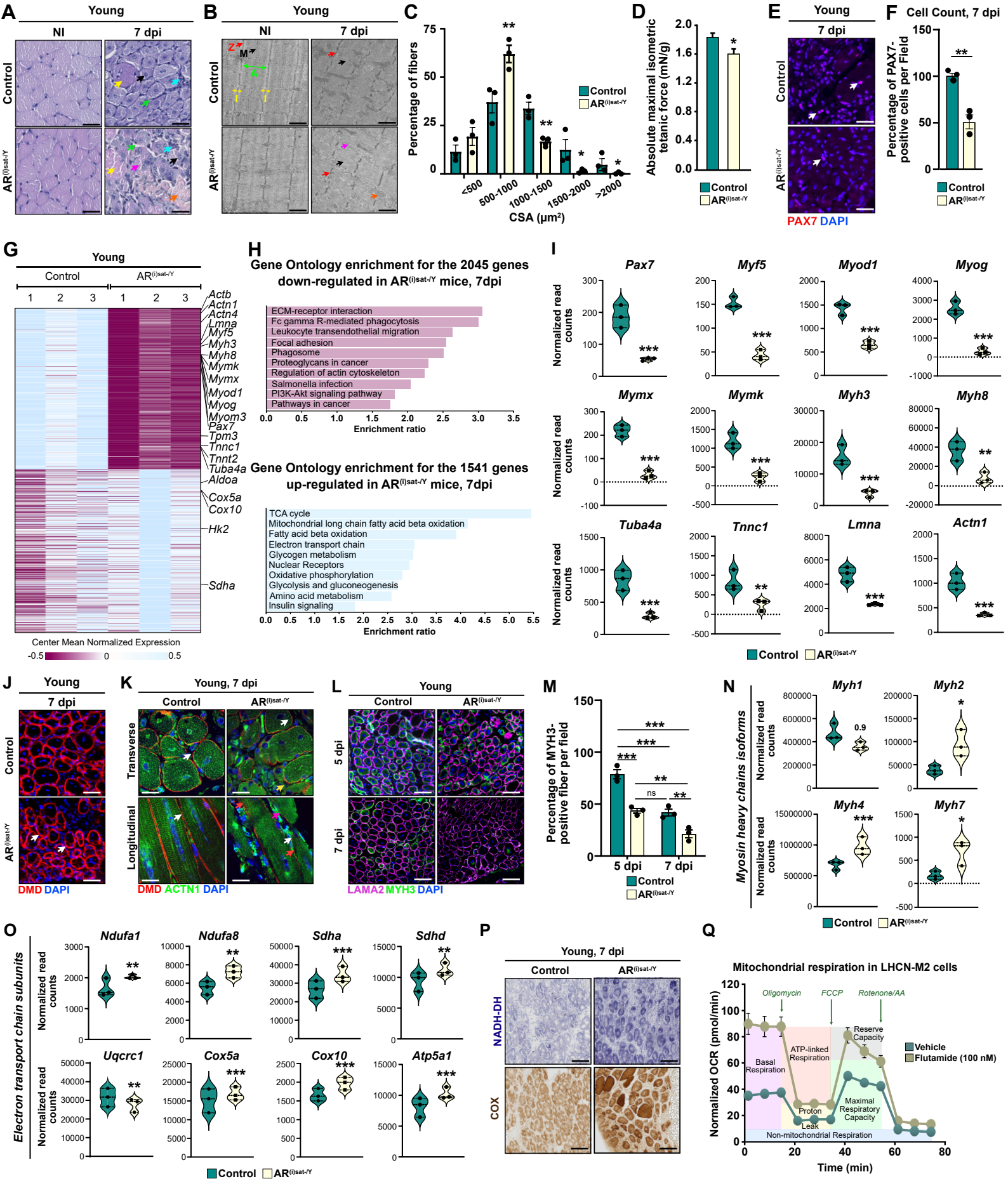
A
Young
NI
7 dpi
Control
AR(i)sat-/Y
B
Young
NI
7 dpi
Control
AR(i)sat-/Y
Z
M
A
I
C
Percentage of fibers
75
50
25
0
**
**
*
*
<500
500-1000
1000-1500
1500-2000
>2000
CSA (µm²)
Control
AR(i)sat-/Y
D
Absolute maximal isometric tetanic force (mN/g)
2.0
1.6
1.2
0.8
0.4
0.0
*
Control
AR(i)sat-/Y
E
Young
7 dpi
Control
AR(i)sat-/Y
PAX7 DAPI
F
Cell Count, 7 dpi
Percentage of PAX7-positive cells per Field
150
100
50
0
**
Control
AR(i)sat-/Y
G
Young
Control
AR(i)sat-/Y
1 2 3 1 2 3
Actb
Actn1
Actn4
Lmna
Myf5
Myh3
Myh8
Mymk
Mymx
Myod1
Myog
Myom3
Pax7
Tpm3
Tnnc1
Tnnt2
Tuba4a
Aldoa
Cox5a
Cox10
Hk2
Sdha
Center Mean Normalized Expression
-0.5
0
0.5
H
Gene Ontology enrichment for the 2045 genes down-regulated in AR(i)sat-/Y mice, 7dpi
ECM-receptor interaction
Fc gamma R-mediated phagocytosis
Leukocyte transendothelial migration
Focal adhesion
Phagosome
Proteoglycans in cancer
Regulation of actin cytoskeleton
Salmonella infection
PI3K-Akt signaling pathway
Pathways in cancer
0.0 0.5 1.0 1.5 2.0 2.5 3.0 3.5
Enrichment ratio
Gene Ontology enrichment for the 1541 genes up-regulated in AR(i)sat-/Y mice, 7dpi
TCA cycle
Mitochondrial long chain fatty acid beta oxidation
Fatty acid beta oxidation
Electron transport chain
Glycogen metabolism
Nuclear Receptors
Oxidative phosphorylation
Glycolysis and gluconeogenesis
Amino acid metabolism
Insulin signaling
0.0 0.5 1.0 1.5 2.0 2.5 3.0 3.5 4.0 4.5 5.0 5.5
Enrichment ratio
I
Pax7
Myf5
Myod1
Myog
Mymx
Mymk
Myh3
Myh8
Tuba4a
Tnnc1
Lmna
Actn1
Normalized read counts
Control
AR(i)sat-/Y
J
Young
7 dpi
Control
AR(i)sat-/Y
DMD DAPI
K
Young, 7 dpi
Control
AR(i)sat-/Y
Transverse
Longitudinal
DMD ACTN1 DAPI
L
Young
Control
AR(i)sat-/Y
5 dpi
7 dpi
LAMA2 MYH3 DAPI
M
Percentage of MYH3-positive fiber per field
150
100
50
0
***
***
***
**
ns
**
5 dpi
7 dpi
Control
AR(i)sat-/Y
N
Myosin heavy chains isoforms
Normalized read counts
Myh1
Myh2
Myh4
Myh7
0.9
Control
AR(i)sat-/Y
O
Electron transport chain subunits
Normalized read counts
Ndufa1
Ndufa8
Sdha
Sdhd
Uqcrc1
Cox5a
Cox10
Atp5a1
Control
AR(i)sat-/Y
P
Young, 7 dpi
Control
AR(i)sat-/Y
NADH-DH
COX
Q
Mitochondrial respiration in LHCN-M2 cells
Oligomycin
FCCP
Rotenone/AA
Normalized OCR (pmol/min)
Basal Respiration
ATP-linked Respiration
Proton Leak
Reserve Capacity
Maximal Respiratory Capacity
Non-mitochondrial Respiration
Vehicle
Flutamide (100 nM)
Time (min)
0 20 40 60 80

FIGURE 2

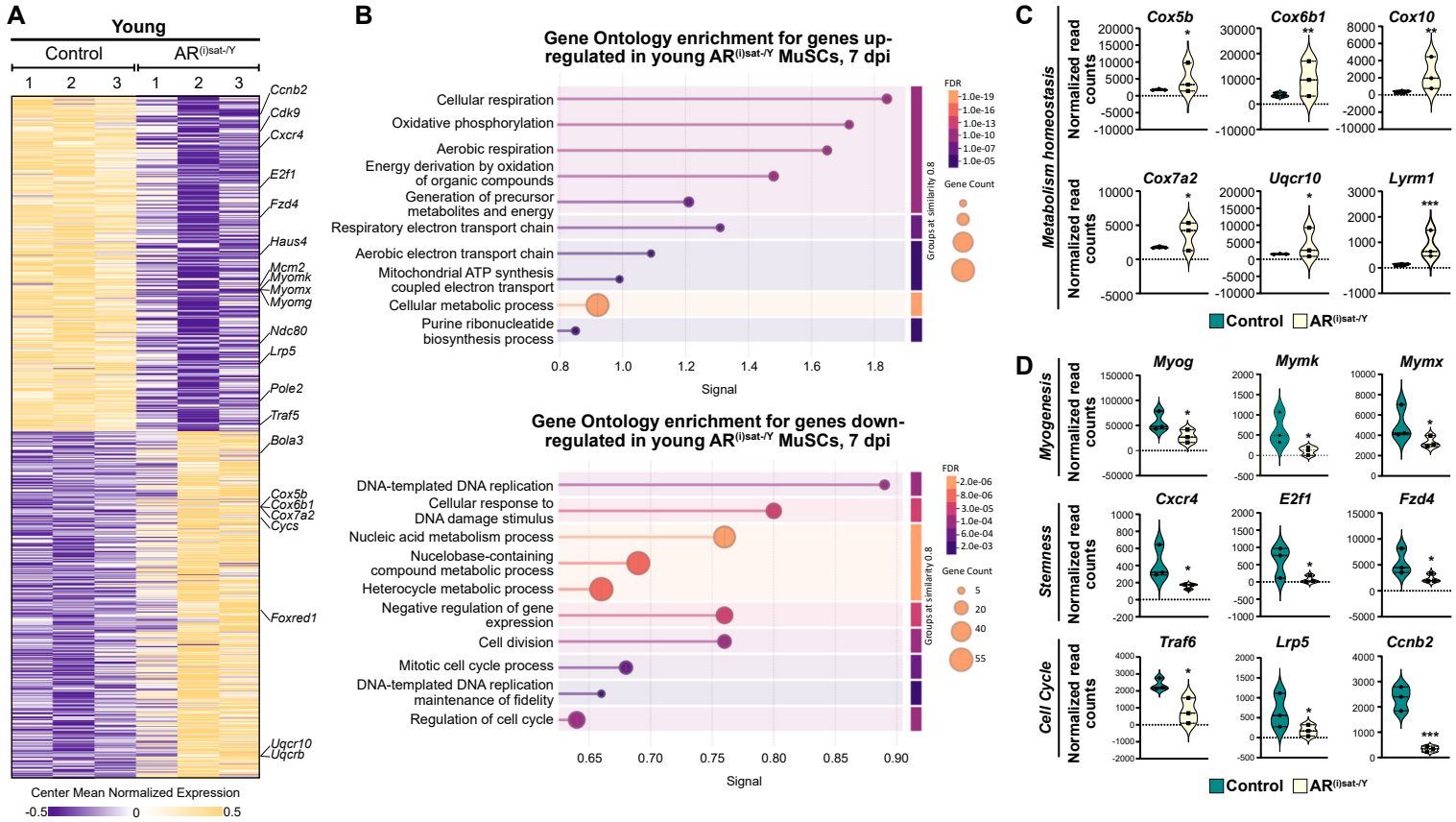

E

AR Known Motif Search

Name	Logo	p-value	% of Targets
ARE		1e-124	49.45 %
AR-half site		1e-17	68.13%

AR *de novo* Motif Search

Name	Logo	p-value	% of Targets
AR		1e-348	47.15 %
AR-half site		1e-13	8.79%

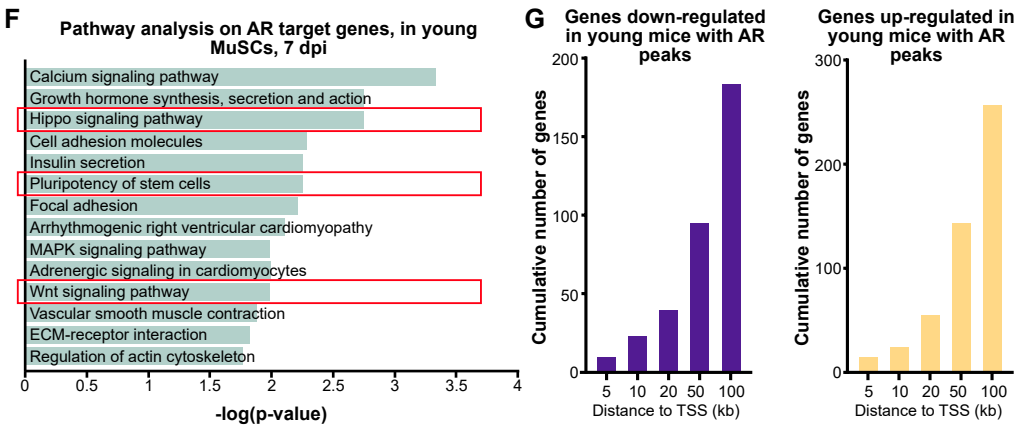

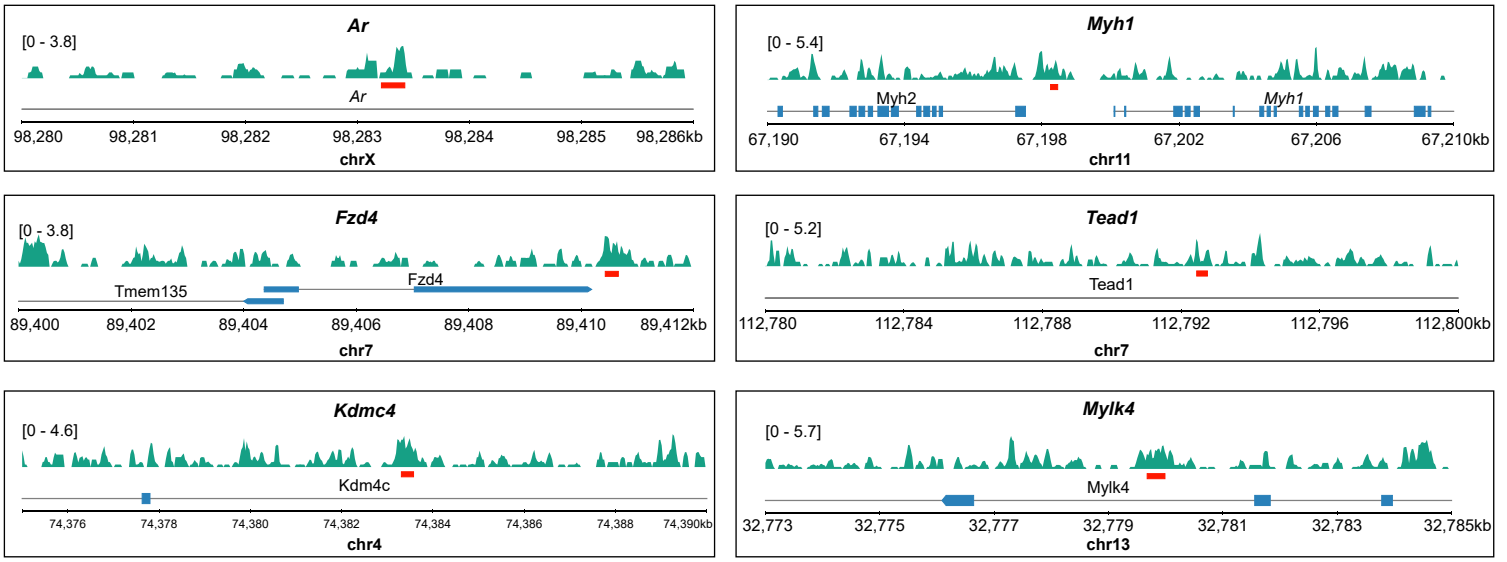

FIGURE 3

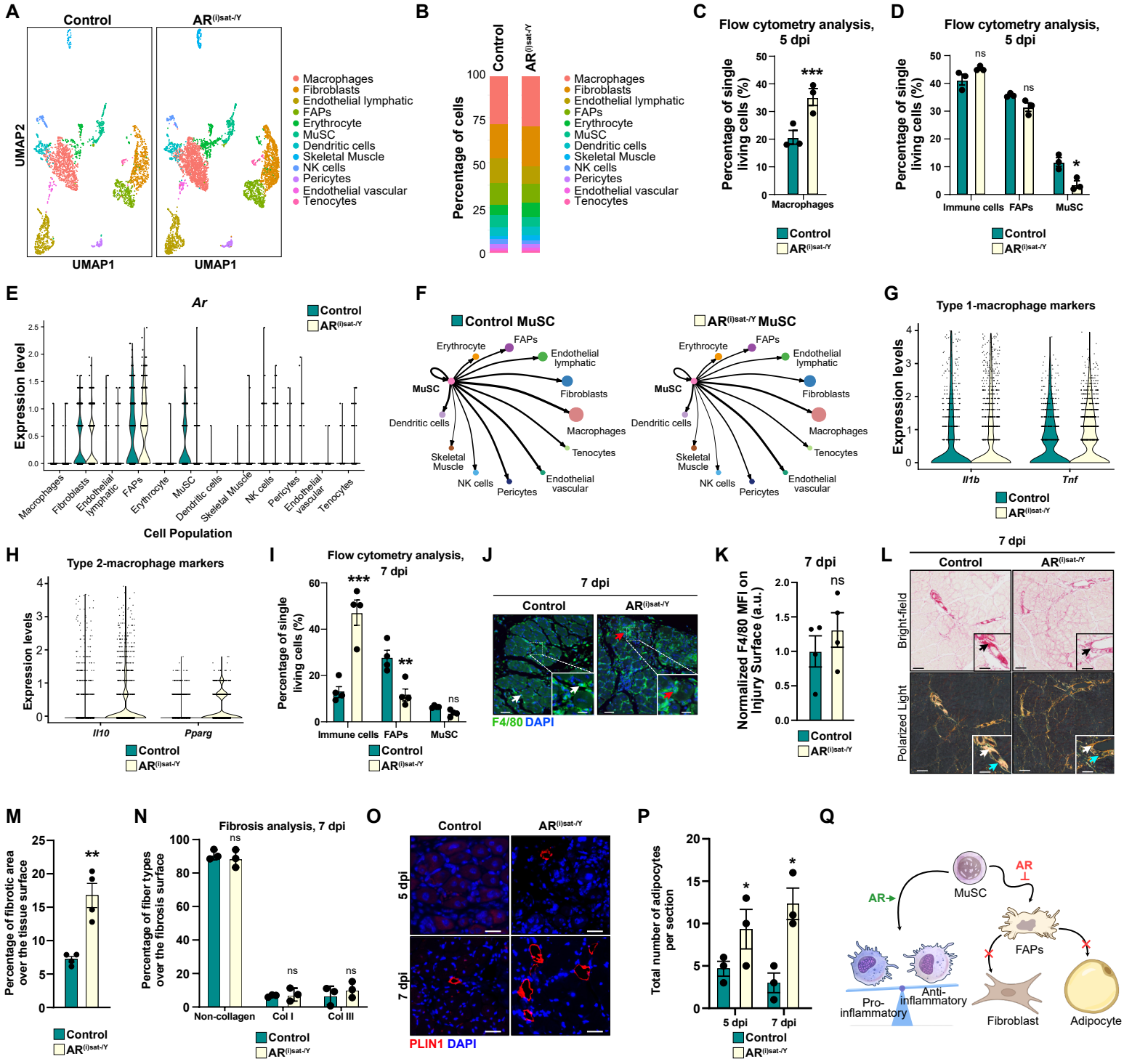
A
Control
AR(i)sat-/Y
UMAP2
UMAP1
UMAP1
Macrophages
Fibroblasts
Endothelial lymphatic
FAPs
Erythrocyte
MuSC
Dendritic cells
Skeletal Muscle
NK cells
Pericytes
Endothelial vascular
Tenocytes
B
Control
AR(i)sat-/Y
Percentage of cells
100
75
50
25
0
C
Flow cytometry analysis, 5 dpi
Percentage of single living cells (%)
***
Macrophages
Control
AR(i)sat-/Y
D
Flow cytometry analysis, 5 dpi
Percentage of single living cells (%)
ns
ns
*
Immune cells
FAPs
MuSC
Control
AR(i)sat-/Y
E
Ar
Control
AR(i)sat-/Y
Expression level
Cell Population
F
Control MuSC
AR(i)sat-/Y MuSC
Erythrocyte
FAPs
Endothelial lymphatic
MuSC
Fibroblasts
Dendritic cells
Macrophages
Tenocytes
Skeletal Muscle
NK cells
Pericytes
Endothelial vascular
G
Type 1-macrophage markers
Expression levels
Il1b
Tnf
Control
AR(i)sat-/Y
H
Type 2-macrophage markers
Expression levels
Il10
Pparg
Control
AR(i)sat-/Y
I
Flow cytometry analysis, 7 dpi
Percentage of single living cells (%)
***
**
ns
Immune cells
FAPs
MuSC
Control
AR(i)sat-/Y
J
7 dpi
Control
AR(i)sat-/Y
F4/80 DAPI
K
7 dpi
Normalized F4/80 MFI on Injury Surface (a.u.)
ns
Control
AR(i)sat-/Y
L
7 dpi
Control
AR(i)sat-/Y
Bright-field
Polarized Light
M
Percentage of fibrotic area over the tissue surface
**
Control
AR(i)sat-/Y
N
Fibrosis analysis, 7 dpi
Percentage of fiber types over the fibrosis surface
ns
ns
ns
Non-collagen
Col I
Col III
Control
AR(i)sat-/Y
O
Control
AR(i)sat-/Y
5 dpi
7 dpi
PLIN1 DAPI
P
Total number of adipocytes per section
*
*
5 dpi
7 dpi
Control
AR(i)sat-/Y
Q
AR
AR
MuSC
FAPs
Pro-inflammatory
Anti-inflammatory
Fibroblast
Adipocyte

FIGURE 4

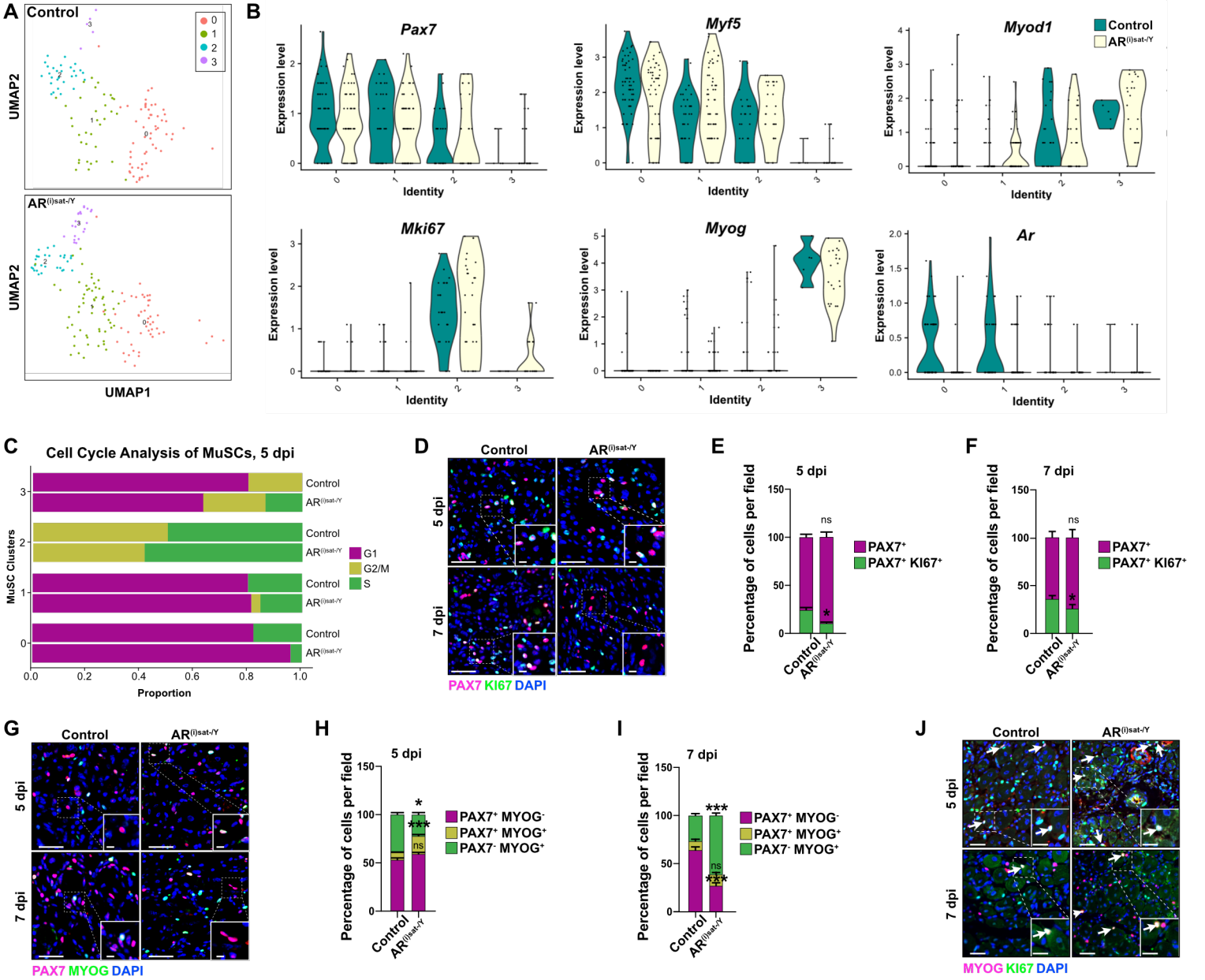
A
Control
AR(i)sat-/Y
UMAP2
UMAP1
B
Pax7
Myf5
Myod1
Mki67
Myog
Ar
Expression level
Identity
Control
AR(i)sat-/Y
C
Cell Cycle Analysis of MuSCs, 5 dpi
MuSC Clusters
Proportion
G1
G2/M
S
D
Control
AR(i)sat-/Y
5 dpi
7 dpi
PAX7 KI67 DAPI
E
5 dpi
Percentage of cells per field
PAX7+
PAX7+ KI67+
ns
F
7 dpi
G
PAX7 MYOG DAPI
H
PAX7+ MYOG-
PAX7+ MYOG+
PAX7- MYOG+
I
J
MYOG KI67 DAPI
K
Number of MYOG/MKI67-positive cells per field
L
Young
M
DMD PAX7 DAPI
N
28+7 dpi
Number of PAX7-positive cells per field
O
MuSC
AR
Maintenance plane
Commitment plane

FIGURE 5

A

AR Known Motif Search

Name	Logo	p-value	% of Targets
ARE		1e-55	26.2 %
AR-half site		1e-68	39.5%

AR *de novo* Motif Search

Name	Logo	p-value	% of Targets
AR	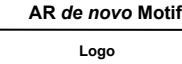	1e-348	47.15 %

B

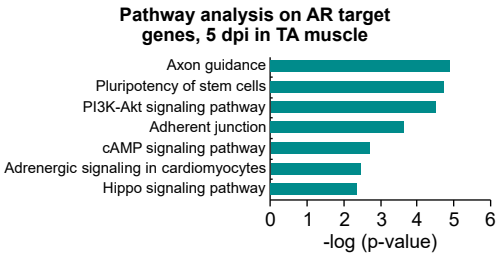

C

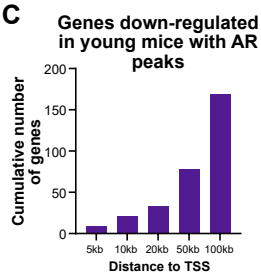

D

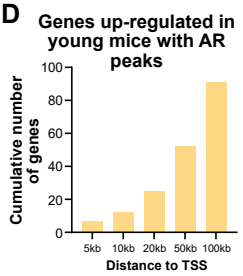

E

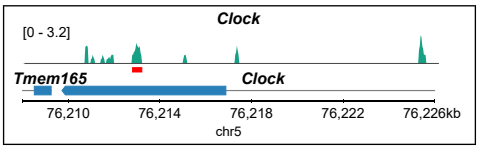

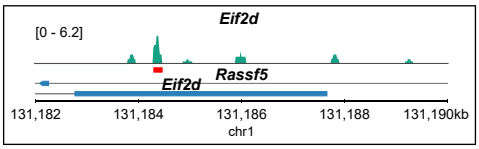

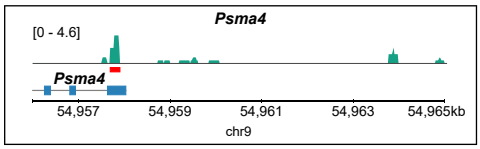

F

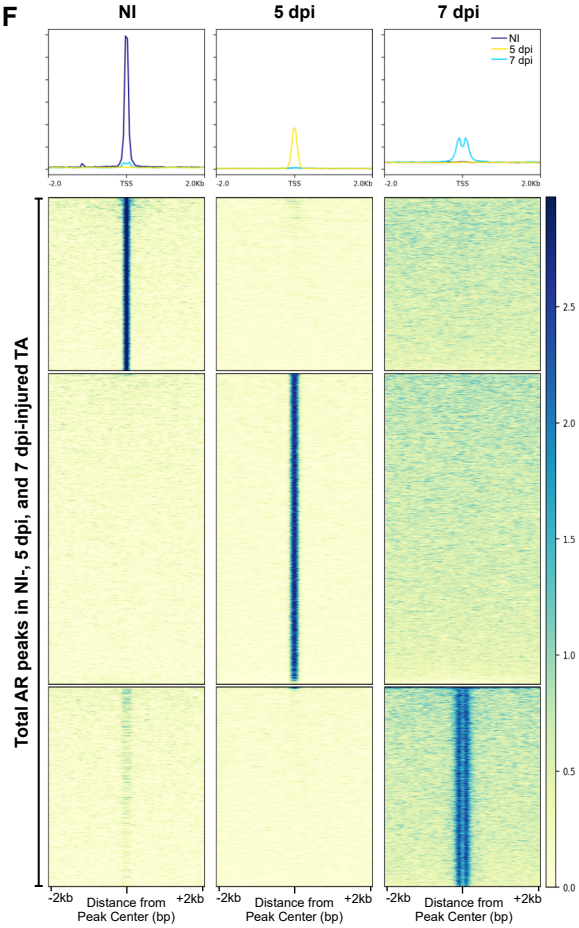

G

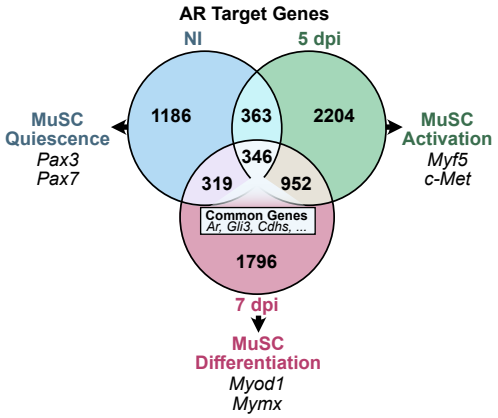

H

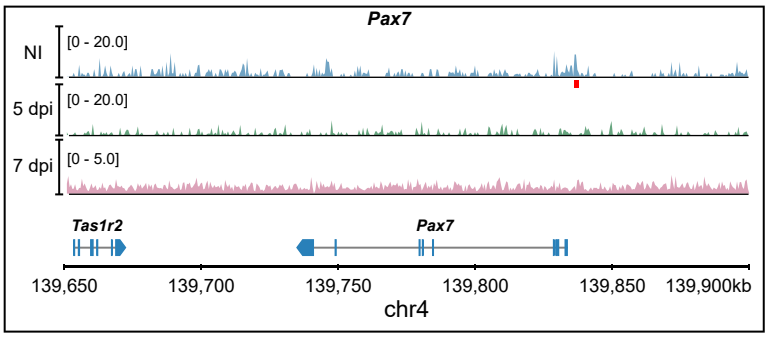

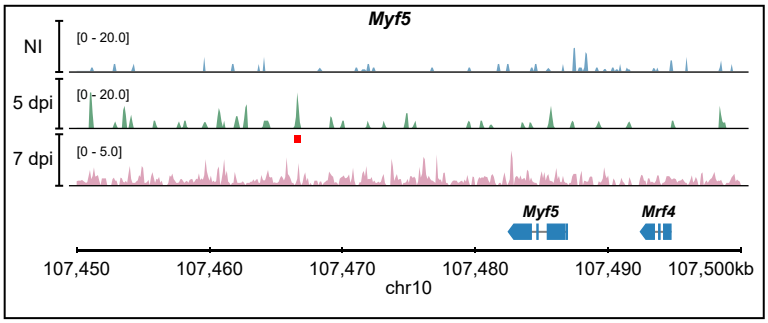

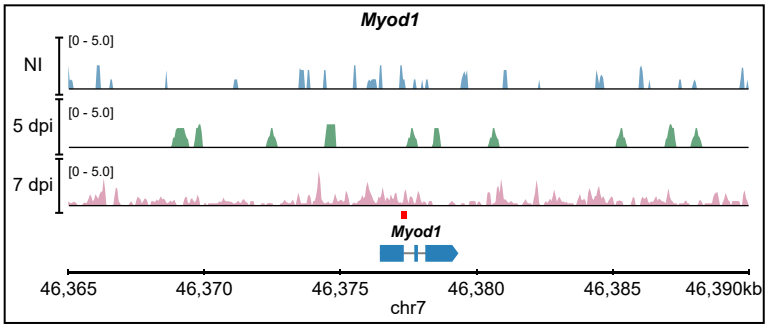

I

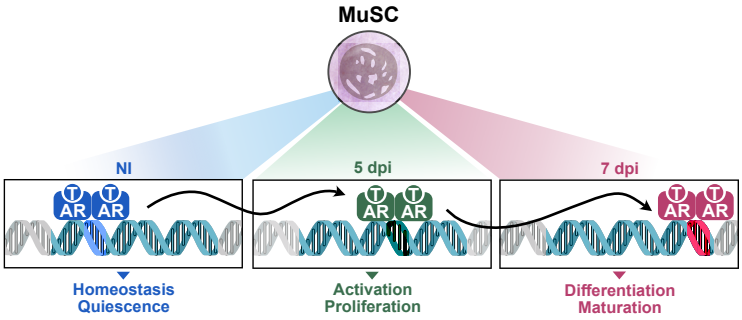

FIGURE 6

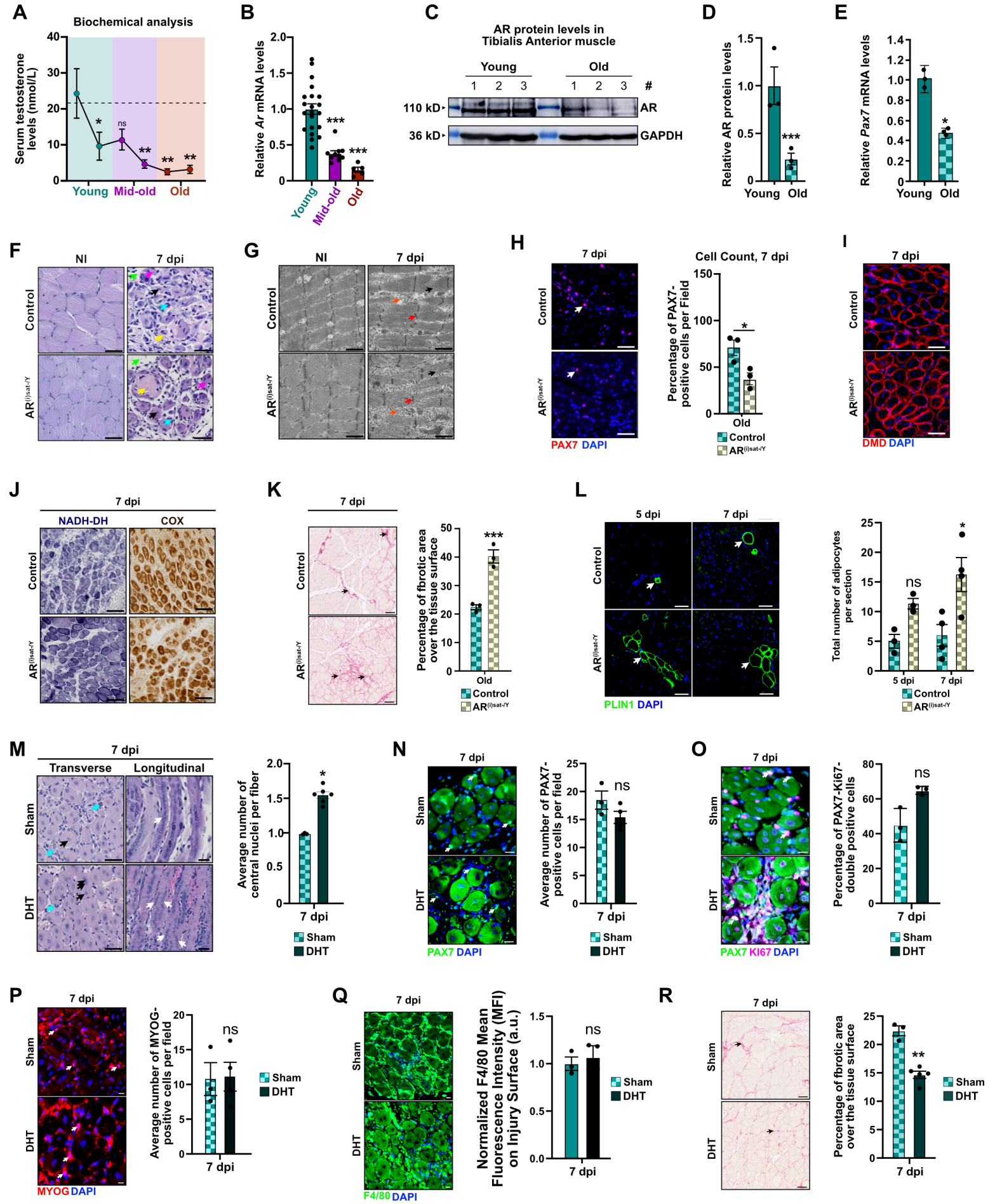
A
Biochemical analysis
Serum testosterone levels (nmol/L)
Young
Mid-old
Old
B
Relative Ar mRNA levels
C
AR protein levels in Tibialis Anterior muscle
Young
Old
110 kD
36 kD
AR
GAPDH
D
Relative AR protein levels
E
Relative Pax7 mRNA levels
F
NI
7 dpi
Control
G
H
Cell Count, 7 dpi
Percentage of PAX7-positive cells per Field
PAX7 DAPI
I
DMD DAPI
J
NADH-DH
COX
K
Percentage of fibrotic area over the tissue surface
L
5 dpi
PLIN1 DAPI
Total number of adipocytes per section
M
Transverse
Longitudinal
Sham
DHT
Average number of central nuclei per fiber
N
Average number of PAX7-positive cells per field
O
PAX7 KI67 DAPI
Percentage of PAX7-KI67-double positive cells
P
MYOG DAPI
Average number of MYOG-positive cells per field
Q
F4/80 DAPI
Normalized F4/80 Mean Fluorescence Intensity (MFI) on Injury Surface (a.u.)
R

FIGURE 7

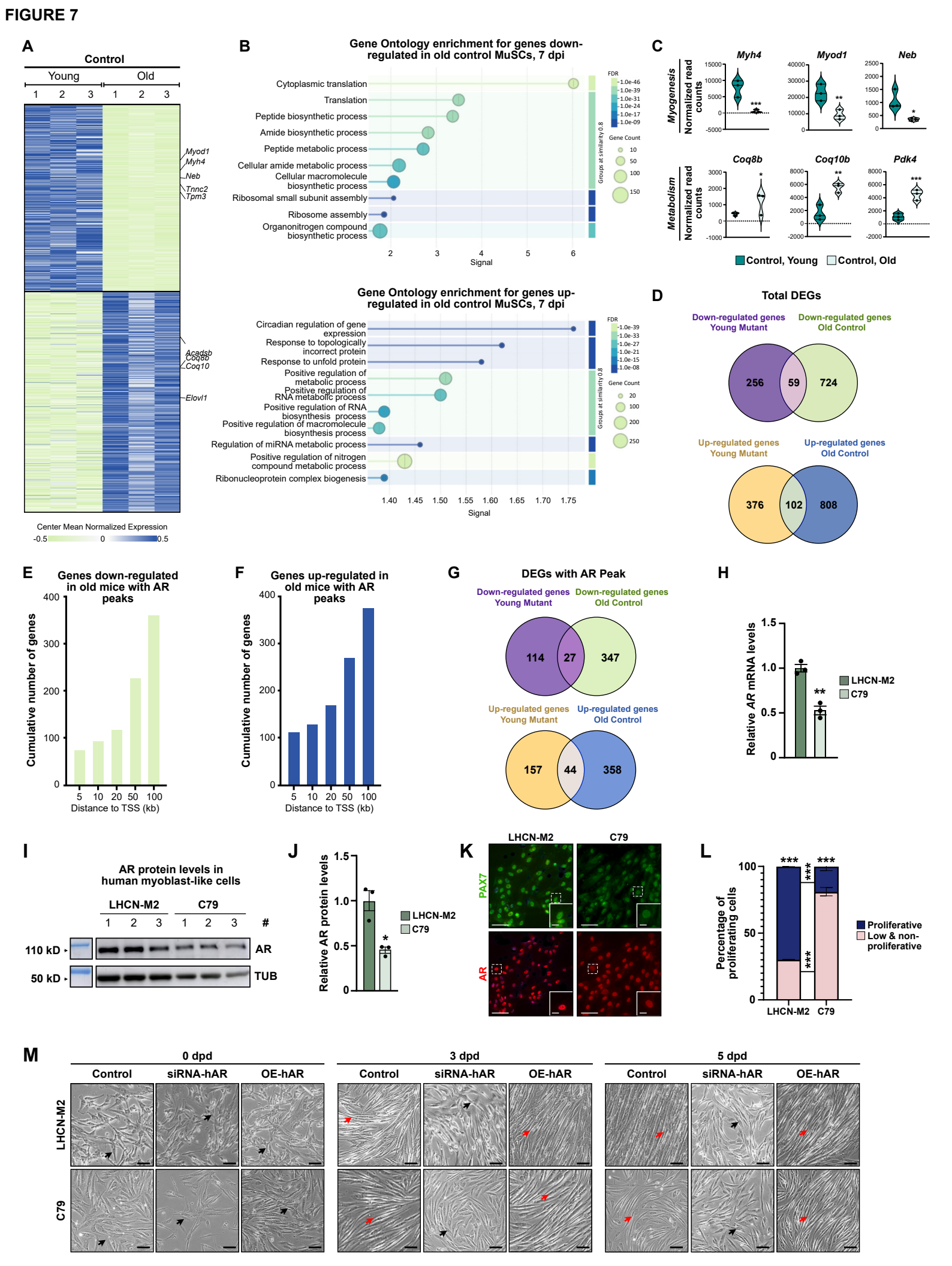
A
Control
Young
Old
1 2 3 1 2 3
Myod1
Myh4
Neb
Tnnc2
Tpm3
Acadsb
Coq8b
Coq10
Elovl1
Center Mean Normalized Expression
-0.5 0 0.5
B
Gene Ontology enrichment for genes down-regulated in old control MuSCs, 7 dpi
Cytoplasmic translation
Translation
Peptide biosynthetic process
Amide biosynthetic process
Peptide metabolic process
Cellular amide metabolic process
Cellular macromolecule biosynthetic process
Ribosomal small subunit assembly
Ribosome assembly
Organonitrogen compound biosynthetic process
Signal
FDR
Gene Count
Groups at similarity 0.8
Gene Ontology enrichment for genes up-regulated in old control MuSCs, 7 dpi
Circadian regulation of gene expression
Response to topologically incorrect protein
Response to unfold protein
Positive regulation of metabolic process
Positive regulation of RNA metabolic process
Positive regulation of RNA biosynthesis process
Positive regulation of macromolecule biosynthesis process
Regulation of miRNA metabolic process
Positive regulation of nitrogen compound metabolic process
Ribonucleoprotein complex biogenesis
C
Myogenesis
Metabolism
Normalized read counts
Myh4
Myod1
Neb
Coq8b
Coq10b
Pdk4
Control, Young
Control, Old
D
Total DEGs
Down-regulated genes Young Mutant
Down-regulated genes Old Control
256 59 724
Up-regulated genes Young Mutant
Up-regulated genes Old Control
376 102 808
E
Genes down-regulated in old mice with AR peaks
Cumulative number of genes
Distance to TSS (kb)
F
Genes up-regulated in old mice with AR peaks
Cumulative number of genes
Distance to TSS (kb)
G
DEGs with AR Peak
Down-regulated genes Young Mutant
Down-regulated genes Old Control
114 27 347
Up-regulated genes Young Mutant
Up-regulated genes Old Control
157 44 358
H
Relative AR mRNA levels
LHCN-M2
C79
I
AR protein levels in human myoblast-like cells
LHCN-M2
C79
110 kD
50 kD
AR
TUB
J
Relative AR protein levels
LHCN-M2
C79
K
LHCN-M2
C79
PAX7
AR
L
Percentage of proliferating cells
Proliferative
Low & non-proliferative
LHCN-M2
C79
M
0 dpd
3 dpd
5 dpd
Control
siRNA-hAR
OE-hAR
LHCN-M2
C79